

Ab Initio Molecular Cavity Quantum Electrodynamics Simulations Using Machine Learning Models

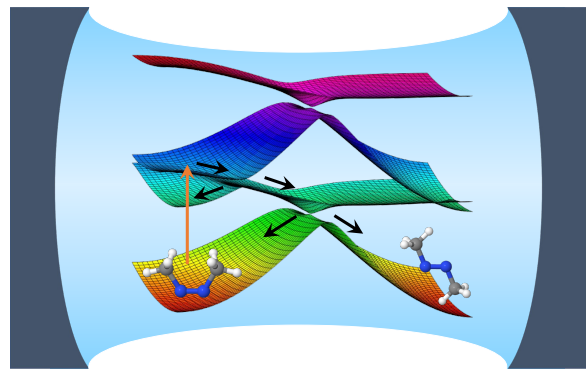
Deping Hu* and Pengfei Huo*

Department of Chemistry, University of Rochester, Rochester, New York 14627, USA

E-mail: deping.hu@rochester.edu; pengfei.huo@rochester.edu

Abstract

We present a mixed quantum-classical simulation of polariton dynamics for molecule-cavity hybrid systems. In particular, we treat the coupled electronic-photonic degrees of freedom (DOFs) as the quantum subsystem and the nuclear DOFs as the classical subsystem and use the trajectory surface hopping approach to simulate non-adiabatic dynamics among the polariton states due to the coupled motion of nuclei. We use the accurate nuclear gradient expression derived from the Pauli-Fierz Quantum Electrodynamics Hamiltonian without making further approximations. The energies, gradients, and derivative couplings of the molecular systems are obtained from the on-the-fly simulations at the level of complete active space self-consistent field (CASSCF), which are used to compute the polariton energies and nuclear gradients. The derivatives of dipoles are also necessary ingredients in the polariton nuclear gradient expression but are often not readily available in electronic structure methods. To address this challenge, we use a machine learning model with the Kernel ridge regression method to construct the dipoles and further obtain their derivatives, at the same level as the CASSCF theory. The cavity loss process is modeled with the Lindblad jump superoperator on the reduced density of the electronic-photonic quantum subsystem. We investigate the azomethane molecule and its photoinduced isomerization dynamics inside the cavity. Our results show the accuracy of the machine-learned dipoles and their usage in simulating polariton dynamics. Our polariton dynamics results also demonstrate the isomerization reaction of azomethane can be effectively tuned by coupling to an optical cavity and by changing the light-matter coupling strength and the cavity loss rate.



1 Introduction

When coupling molecules with quantized radiation modes inside an optical cavity, a set of new photon-matter hybrid states are created due to the coupling between the molecules and the quantized radiation field.^{1–7} These new created hybrid states, which are commonly referred to as polaritons, have been shown to facilitate new chemical reactivities and selectivities.^{1,6,8–10} Theoretical investigations play a crucial role in understanding the fundamental limit and basic principles in this emerging field,^{5,6,11–17} as these polariton chemical reactions often involve a rich dynamical interplay among the electronic, nuclear, and photonic degrees of freedom (DOFs).

Recently, various theoretical methods have been developed or extended to directly simulate the polariton dynamics. These include the full quantum dynamics simulations,^{18–21} mixed-quantum-classical (MQC) dynamics,^{12,13,22–25} and non-adiabatic dynamics based on the mapping formalism.^{6,26} Among them, the MQC dynamics methods describe the electronic-photonic DOFs quantum mechanically and treat the nuclear DOFs classically, hence well balance the computational cost and accuracy of the dynamics. Thus, the MQC methods, including the Ehrenfest and trajectory surface hopping (TSH) methods, have been widely used in the non-adiabatic polariton dynamics recently.^{11–17,23–28}

In the propagation of the polariton dynamics with the MQC methods, besides the energies of the electron-

photon hybrid states, we need to derive the nuclear gradients and the couplings between these states, where the derivatives of molecular dipoles (including permanent dipoles and transition dipoles) are the key ingredients.^{25,26} For some model systems with well-defined diabatic electronic states, the dipoles of/between these diabatic states can be set to constants.^{23,28} For model systems with adiabatic electronic states, the dipoles of/between these adiabatic states can be calculated through the discrete variable representation (DVR).^{25,26} Evaluating the derivatives of molecular dipoles remains a theoretical bottleneck for simulating *ab initio* polariton quantum dynamics. These derivatives are neither readily available for most electronic structure methods nor computationally cheap to obtain.

Recent polariton quantum dynamics simulations are focusing on obtaining these expensive derivatives using semi-empirical electronic structure methods. For example, Zhang *et al.* derived the derivative of transition dipoles at the AM1/CIS level of theory²² and applied it to the TSH simulations of stilbene molecule coupled to the cavity based on the Jaynes-Cummings (JC)²⁹ and Tavis-Cummings (TC) models. Fregoni *et al.* derived the derivative of transition dipoles at the AM1/FOMO-CI level and performed the TSH simulations for azobenzene molecule based on the Rabi-type model (that excludes the permanent dipole moment and dipole self-energy).^{13,15,27} Groenhof *et al.* approximated transition dipoles by a first-order Taylor expansion around the ground state equilibrium and obtained the derivatives through least-squares fitting with a large number geometrical conformations.^{12,14,16,17} The lack of accurate derivatives on dipoles (at the correlated wavefunction level of theory) had become the major theoretical bottleneck in performing *ab initio* on-the-fly simulations of polariton chemistry. To the best of our knowledge, there is no previous work on using correlated wavefunction level of theory to perform *ab initio* on-the-fly quantum dynamics simulations of polariton chemistry with the rigorous nuclear gradient.²⁵

In this work, we construct the dipoles (including permanent and transition dipoles) and their derivatives for realistic molecules using machine-learning techniques.^{30–34} We apply the machine-learned dipoles and derivatives to *ab initio* on-the-fly polariton dynamics simulations of a realistic polyatomic molecular system, azomethane, coupled to an optical cavity. We use the accurate nuclear gradient expression derived from the Pauli-Fierz (PF) Quantum Electrodynamics Hamiltonian without making further approximations.²⁵ The energies, gradients, and derivative couplings of the molecular systems are obtained from the on-the-fly simulations at the level of complete active space self-consistent field (CASSCF), which are used to compute the polariton energies and nuclear gradients. The derivatives of dipoles are obtained from the machine learning model, which is trained with the data obtained from the CASSCF level of electronic structure calculations. The

cavity loss process is modeled with the Lindblad jump superoperator on the reduced density of the electronic-photonic quantum subsystem. Our results show the accuracy of the machine-learned dipoles and their usage in simulating polariton dynamics.

We perform the TSH simulations to investigate the photoisomerization reaction inside the cavity. The photoinduced non-adiabatic dynamics process of azomethane has been widely investigated.^{35–39} Since azomethane is the simplest azoalkane and has rich dynamics (*i.e.*, photoisomerization and photodissociation), it is also often used as a model molecular system to test the performance of the non-adiabatic dynamics methods⁴⁰ or the electrical structure methods⁴¹ in the non-adiabatic dynamics simulations. Thus, we adopt azomethane in this work to see how the light-matter coupling can affect the photoinduced reaction of the molecular system. Our polariton dynamics results also demonstrate the isomerization reaction of azomethane can be effectively tuned by coupling to an optical cavity. The machine learning model developed in this work illustrates its potential applications in the polariton dynamics simulations, where we can in principle construct the derivatives of dipoles for molecules with any electronic structure method if that method can provide the dipoles. This development paves the way toward simulating complex molecular systems inside an optical cavity.

2 Theoretical Approaches

2.1 Quantum Electrodynamics Hamiltonian

The Pauli-Fierz (PF) QED Hamiltonian for one molecule coupled to a quantized radiation field inside an optical cavity is expressed as

$$\hat{H} = \hat{T}_n + \hat{H}_{pl}, \quad (1)$$

where \hat{T}_n represents the nuclear kinetic energy operator. Further, \hat{H}_{pl} is commonly referred to as the polariton Hamiltonian^{3,42} and is defined as

$$\hat{H}_{pl} \equiv \hat{H}_{en} + \hat{H}_p + \hat{H}_{enp} + \hat{H}_d, \quad (2)$$

where \hat{H}_{en} is the electronic Hamiltonian that describes electron-nucleus interactions. In addition, \hat{H}_p , \hat{H}_{enp} , and \hat{H}_d represent the photonic Hamiltonian, electronic-nuclear-photonic interactions, and the dipole self-energy (DSE) term, respectively.

The electronic-nuclear potential \hat{H}_{en} , which describes the common molecular Hamiltonian (excluding the nu-

clear kinetic energy) is described as follows

$$\hat{H}_{\text{en}} = \hat{T}_e + \hat{V}_{ee} + \hat{V}_{en} + \hat{V}_{nn}. \quad (3)$$

The above expression includes electronic kinetic energy \hat{T}_e , electron-electron interaction \hat{V}_{ee} , electron-nucleus interaction \hat{V}_{en} , and nucleus-nucleus interaction \hat{V}_{nn} . Modern electronic structure theories have been developed around solving the eigenvalue problem of \hat{H}_{en} , providing the following electronically adiabatic energy and its corresponding state

$$\hat{H}_{\text{en}}|\phi_\alpha(\mathbf{R})\rangle = E_\alpha(\mathbf{R})|\phi_\alpha(\mathbf{R})\rangle. \quad (4)$$

Here, $|\phi_\alpha(\mathbf{R})\rangle$ represents the α_{th} many-electron adiabatic state for a given molecular system, with the adiabatic energy $E_\alpha(\mathbf{R})$.

For clarity, we restrict our discussions to the cavity with only one photonic mode, and all the formulas presented here can be easily generalized into a more realistic, many-mode cavity. The photonic Hamiltonian is written as

$$\hat{H}_p = \frac{1}{2} (\hat{p}_c^2 + \omega_c^2 \hat{q}_c^2) = \hbar \omega_c \left(\hat{a}^\dagger \hat{a} + \frac{1}{2} \right), \quad (5)$$

where $\hat{q}_c = \sqrt{\hbar/2\omega_c}(\hat{a}^\dagger + \hat{a})$ and $\hat{p}_c = i\sqrt{\hbar\omega_c/2}(\hat{a}^\dagger - \hat{a})$ are photon field operators, \hat{a}^\dagger and \hat{a} are the photonic creation and annihilation operators, respectively, and ω_c is the photon frequency inside the cavity.

The light-matter coupling term \hat{H}_{enp} (electronic-nuclear-photonic interactions) under the dipole gauge (and the long wavelength approximation) is expressed as

$$\hat{H}_{\text{enp}} = \omega_c \hat{q}_c (\boldsymbol{\lambda} \cdot \hat{\boldsymbol{\mu}}) = g_c \boldsymbol{\epsilon} \cdot \hat{\boldsymbol{\mu}} (\hat{a}^\dagger + \hat{a}), \quad (6)$$

where $\boldsymbol{\lambda} = \lambda \cdot \boldsymbol{\epsilon}$ characterizes the cavity photon field strength, $\boldsymbol{\epsilon}$ is the direction of the field polarization, which can be written as

$$\boldsymbol{\epsilon} = \epsilon_x \mathbf{x} + \epsilon_y \mathbf{y} + \epsilon_z \mathbf{z}, \quad (7)$$

where \mathbf{x} , \mathbf{y} , and \mathbf{z} are the unit vectors in the X, Y, and Z directions, respectively. These directions are related to the cavity structure. For convenience, we also use these directions to define reference coordinate systems for all initial nuclear geometries, see Sec 4.2 (Fig. 2a) for details. The cavity field strength is determined by the volume of the cavity as $\lambda = \sqrt{1/\varepsilon_0 V_0}$, where ε_0 is the permittivity inside the cavity and V_0 is the effective quantization volume inside the cavity. Another commonly used light-matter coupling strength is characterized as $g_c = \sqrt{\hbar\omega_c/2}\lambda$. Further, the total dipole operator of both electrons and nuclei is defined as

$$\hat{\boldsymbol{\mu}} = - \sum_i e \hat{\mathbf{r}}_i + \sum_j Z_j e \hat{\mathbf{R}}_j, \quad (8)$$

where $-e$ is the charge of the electron and $Z_j e$ is the charge of the j_{th} nucleus. Finally, the dipole self-energy

(DSE) term is expressed as

$$\hat{H}_d = \frac{1}{2} (\boldsymbol{\lambda} \cdot \hat{\boldsymbol{\mu}})^2 = \frac{g_c^2}{\hbar \omega_c} (\boldsymbol{\epsilon} \cdot \hat{\boldsymbol{\mu}})^2. \quad (9)$$

For the molecule-cavity hybrid system, we use the convenient photon-dressed electronic adiabatic states

$$|\psi_i(\mathbf{R})\rangle = |\phi_\alpha(\mathbf{R})\rangle \otimes |n\rangle \equiv |\phi_\alpha(\mathbf{R}), n\rangle, \quad (10)$$

where quantum number $i \equiv \{\alpha, n\}$ indicates both the adiabatic electronic state of the molecule and the Fock state. We refer to $|\psi_i(\mathbf{R})\rangle$ as the adiabatic-Fock state in this work. Note that we have introduced a shorthand notation in Eq. 10, which will be used throughout the rest of this paper. This is one of the most straightforward choices of basis for the hybrid system because of the readily available adiabatic electronic information (*e.g.*, wavefunctions, energies, and the dipole matrix) from electronic structure calculations.

With the adiabatic-Fock state basis $|\phi_\nu(\mathbf{R}), n\rangle$ and $|\phi_\gamma(\mathbf{R}), m\rangle$ introduced in Eq. 10, the matrix elements of all terms in Eq. 2 can be explicitly expressed as follows (using the properties of creation and annihilation operators of photonic DOF)

$$\langle \phi_\gamma(\mathbf{R}), m | \hat{H}_{\text{en}} | \phi_\nu(\mathbf{R}), n \rangle = E_\nu(\mathbf{R}) \delta_{\gamma,\nu} \delta_{m,n} \quad (11a)$$

$$\langle \phi_\gamma(\mathbf{R}), m | \hat{H}_p | \phi_\nu(\mathbf{R}), n \rangle = \hbar \omega_c (m + \frac{1}{2}) \delta_{\gamma,\nu} \delta_{m,n} \quad (11b)$$

$$\langle \phi_\gamma(\mathbf{R}), m | \hat{H}_{\text{enp}} | \phi_\nu(\mathbf{R}), n \rangle \quad (11c)$$

$$= g_c \boldsymbol{\epsilon} \cdot \boldsymbol{\mu}_{\gamma\nu}(\mathbf{R}) (\sqrt{n} \delta_{m,n-1} + \sqrt{n+1} \delta_{m,n+1}) \quad (11d)$$

$$\langle \phi_\gamma(\mathbf{R}), m | \hat{H}_d | \phi_\nu(\mathbf{R}), n \rangle = \frac{g_c^2}{\hbar \omega_c} \sum_\xi (\boldsymbol{\epsilon} \cdot \boldsymbol{\mu}_{\gamma\xi}(\mathbf{R}) (\boldsymbol{\epsilon} \cdot \boldsymbol{\mu}_{\xi\nu}(\mathbf{R})) \delta_{m,n} \equiv D_{\gamma\nu}^2(\mathbf{R}),$$

where $E_\nu(\mathbf{R})$ and $\boldsymbol{\mu}_{\gamma\nu}(\mathbf{R})$ explicitly depend on nuclear position \mathbf{R} . A detailed derivation of these expressions can be found in Ref. 26. In Eq. 11, we have used the matrix element of the dipole operator $\hat{\boldsymbol{\mu}}$ (Eq. 8) under the adiabatic representation

$$\boldsymbol{\mu}_{\gamma\nu}(\mathbf{R}) \equiv \langle \phi_\gamma(\mathbf{R}) | \hat{\boldsymbol{\mu}} | \phi_\nu(\mathbf{R}) \rangle. \quad (12)$$

The total dipole operator $\hat{\boldsymbol{\mu}}$ is a vector that can be projected into the three-dimensional space (of the cavity polarization vector $\boldsymbol{\epsilon}$ (Eq. 7) as follows

$$\hat{\boldsymbol{\mu}} = \hat{\mu}_x \mathbf{x} + \hat{\mu}_y \mathbf{y} + \hat{\mu}_z \mathbf{z}, \quad (13)$$

and Eq. 12 can be further written as

$$\boldsymbol{\mu}_{\gamma\nu}(\mathbf{R}) = \mu_{\gamma\nu}^x(\mathbf{R}) \mathbf{x} + \mu_{\gamma\nu}^y(\mathbf{R}) \mathbf{y} + \mu_{\gamma\nu}^z(\mathbf{R}) \mathbf{z}, \quad (14)$$

where

$$\mu_{\gamma\nu}^l(\mathbf{R}) = \langle \phi_\gamma(\mathbf{R}) | \hat{\mu}_l | \phi_\nu(\mathbf{R}) \rangle, \quad (l = x, y, z). \quad (15)$$

Here $\mu_{\gamma\nu}^l(\mathbf{R})$ are the permanent dipoles ($\gamma = \nu$) and transition dipoles ($\gamma \neq \nu$) along different directions

and are usually obtained from the *ab initio* electronic structure calculation for the realistic molecular system. Combining Eq. 7 and Eq. 14, the light-matter coupling term $\epsilon \cdot \mu_{\gamma\nu}(\mathbf{R})$ in Eq. 11 can be expressed as

$$\epsilon \cdot \mu_{\gamma\nu}(\mathbf{R}) = \epsilon_x \mu_{\gamma\nu}^x(\mathbf{R}) + \epsilon_y \mu_{\gamma\nu}^y(\mathbf{R}) + \epsilon_z \mu_{\gamma\nu}^z(\mathbf{R}). \quad (16)$$

Besides the adiabatic-Fock state, one can further define the polaritonic state^{3,42} as the eigenstate of \hat{H}_{pl} (see definition in Eq. 2) through the following eigenequation

$$\hat{H}_{\text{pl}}|\mathcal{E}_J(\mathbf{R})\rangle = \mathcal{E}_J(\mathbf{R})|\mathcal{E}_J(\mathbf{R})\rangle, \quad (17)$$

where $|\mathcal{E}_J(\mathbf{R})\rangle$ is the polariton state with polariton energy $\mathcal{E}_J(\mathbf{R})$. The polariton eigenstate can be expressed as the linear combination of the adiabatic-Fock states

$$|\mathcal{E}_J(\mathbf{R})\rangle = \sum_{\alpha,n} c_{\alpha,n}^J(\mathbf{R}) |\phi_\alpha(\mathbf{R}), n\rangle, \quad (18)$$

where $c_{\alpha,n}^J(\mathbf{R}) = \langle \phi_\alpha(\mathbf{R}), n | \mathcal{E}_J(\mathbf{R}) \rangle$ and $\mathcal{E}_J(\mathbf{R})$ can be obtained by diagonalizing the matrix of $\hat{V} = \hat{H}_{\text{pl}}$ (constructed from the adiabatic-Fock state basis in Eq. 10 and 11) as

$$\mathbf{U}^\dagger [V(\mathbf{R})] \mathbf{U} = [\mathcal{E}(\mathbf{R})], \quad (19)$$

where

$$[V(\mathbf{R})]_{ij} = \langle \psi_i(\mathbf{R}) | \hat{V} | \psi_j(\mathbf{R}) \rangle, \quad (20)$$

with the basis $|\psi_j(\mathbf{R})\rangle$ defined in Eq. 10.

2.2 Quantum Dynamics Propagation

In this work, we use the TSH approach to propagate the quantum dynamics of the coupled electronic-photonic-nuclear DOFs. In particular, the electronic-photonic DOFs are treated as the quantum subsystem, whereas the nuclear DOFs are treated as the classical subsystem. To model the cavity loss (due to the imperfect cavity mirror that leads to a finite photon lifetime), we employ the Lindblad dynamics approach.^{28,43,44}

The equation of motion (EOM) for the quantum subsystem (electronic-photonic DOF) is expressed as

$$\begin{aligned} \frac{d\hat{\rho}}{dt} &= -\frac{i}{\hbar} [\hat{V}(\mathbf{R}(t)), \hat{\rho}] + \Gamma \left(\hat{L}\hat{\rho}\hat{L}^\dagger - \frac{1}{2} \{ \hat{L}^\dagger \hat{L}, \hat{\rho} \} \right) \\ &\equiv \mathcal{L}_{\hat{V}}[\hat{\rho}] + \mathcal{L}_{\hat{L}}[\hat{\rho}], \end{aligned} \quad (21)$$

where $\hat{\rho}$ is the reduced density operator of the quantum subsystem (electronic-photonic DOFs), $\hat{V} = \hat{H}_{\text{pl}}$ is the polariton Hamiltonian defined in Eq. 2, and \hat{L} is a Lindblad jump operator²⁸ that imparts the impact of the environment (photonic bath) onto the system (cavity mode) with interaction strength Γ (that has a unit of rate or inverse time) and $\{\hat{A}, \hat{B}\} = \hat{A}\hat{B} + \hat{B}\hat{A}$ represents the anti-commutator. In Eq. 21, we further define two superoperators, $\mathcal{L}_{\hat{V}}[\cdot]$ and $\mathcal{L}_{\hat{L}}[\cdot]$, which are used to describe the evolution of reduced density governed by the quantum subsystem Hamiltonian \hat{V} and jump operator \hat{L} , respectively. The Lindblad jump approach ensures

the total population conservation as well as the proper decoherence dynamics among states due to the population jumps.²⁸ For the cavity loss process considered in this work, the jump operator \hat{L} is defined as²⁸

$$\hat{L} = \hat{a} \otimes \hat{\mathcal{I}} = \left[\sum_{n=1}^{\infty} \sqrt{n} |n-1\rangle \langle n| \right] \otimes \hat{\mathcal{I}}, \quad (22)$$

where \hat{a} is the photonic annihilation operator, $\hat{\mathcal{I}}$ is the identity in the electronic subspace. The above jump operator \hat{L} only acts on the photonic DOFs with no impact on the electronic DOFs.

Considering a short-time propagation from t to $t+dt$ where dt is small, the time evolution of the density can be approximated as²⁸

$$\hat{\rho}(t+dt) = e^{(\mathcal{L}_{\hat{V}} + \mathcal{L}_{\hat{L}})dt} [\hat{\rho}(t)] \approx e^{\mathcal{L}_{\hat{L}} dt} e^{\mathcal{L}_{\hat{V}} dt} [\hat{\rho}(t)]. \quad (23)$$

Under the above approximation, we can propagate the density governed by the quantum subsystem Hamiltonian \hat{V} and jump operator \hat{L} separately, with EOMs as

$$\frac{d\hat{\rho}}{dt} = -\frac{i}{\hbar} [\hat{V}(\mathbf{R}(t)), \hat{\rho}] \quad (24a)$$

$$\frac{d\hat{\rho}}{dt} = \Gamma \left(\hat{L}\hat{\rho}\hat{L}^\dagger - \frac{1}{2} \{ \hat{L}^\dagger \hat{L}, \hat{\rho} \} \right). \quad (24b)$$

With the adiabatic-Fock state defined in Eq. 10, the total wavefunction of the quantum subsystem is expanded as

$$|\Psi(\mathbf{r}; \mathbf{R}(t))\rangle = \sum_i c_i(t) |\psi_i(\mathbf{R}(t))\rangle, \quad (25)$$

where $c_i(t)$ is the expansion coefficient. The reduced density matrix element in the adiabatic-Fock state basis can be expressed as follows

$$\rho_{ij}(t) = c_i(t) c_j^*(t). \quad (26)$$

Further, the quantum subsystem evolution equations (Eq. 24a) and (Eq. 24b) are also expanded in this adiabatic-Fock state basis as follows

$$\dot{\rho}_{ij}(t) = -\frac{i}{\hbar} \sum_k (V_{ik} \rho_{kj}(t) - \rho_{ik}(t) V_{kj}) \quad (27a)$$

$$+ \sum_k (\rho_{ik}(t) \mathbf{d}_{kj} \cdot \dot{\mathbf{R}} - \mathbf{d}_{ik} \cdot \dot{\mathbf{R}} \rho_{kj}(t))$$

$$\begin{aligned} \dot{\rho}_{ij}(t) &= \Gamma \sum_k \sum_s \left(L_{ik} \rho_{ks}(t) L_{sj}^\dagger - \frac{1}{2} L_{ik}^\dagger L_{ks} \rho_{sj}(t) \right. \\ &\quad \left. - \frac{1}{2} \rho_{ik}(t) L_{ks}^\dagger L_{sj} \right). \end{aligned} \quad (27b)$$

In the above equations, \mathbf{d}_{ij} is the non-adiabatic coupling (NAC) defined as

$$\mathbf{d}_{ij} = \langle \psi_i(\mathbf{R}) | \nabla | \psi_j(\mathbf{R}) \rangle. \quad (28)$$

We can write the matrix elements of \mathbf{d} in the adiabatic-

Fock state basis as

$$\mathbf{d}_{\gamma m, \nu n} \equiv \langle \phi_\gamma(\mathbf{R}), m | \nabla | \phi_\nu(\mathbf{R}), n \rangle = \mathbf{d}_{\gamma \nu} \delta_{mn}, \quad (29)$$

because the Fock states do not explicitly depend upon \mathbf{R} and are orthonormal to each other, and $\mathbf{d}_{\gamma \nu}$ is the regular NACs among the adiabatic electronic states of the molecule. Further, $\dot{\mathbf{R}}$ is the velocity of the nuclear DOF. The matrix element of the jump operator \hat{L} can also be written in the adiabatic-Fock state basis as

$$\begin{aligned} L_{\gamma m, \nu n} &\equiv \langle \phi_\gamma(\mathbf{R}), m | \left[\sum_{n=1}^{\infty} \sqrt{n} |n-1\rangle \langle n| \right] \otimes \hat{\mathcal{I}} | \phi_\nu(\mathbf{R}), n \rangle \\ &= \sqrt{n} \delta_{m(n-1)} \delta_{\gamma \nu}. \end{aligned} \quad (30)$$

Note that only the propagation of the quantum subsystem is presented above, while the nuclear DOFs are treated classically and propagated using the TSH method, see details in Sec. 2.3.

2.3 Trajectory Surface Hopping

In this work, we use the TSH^{45,46} method to perform the on-the-fly non-adiabatic dynamics for the realistic molecular system coupled to the cavity. Here, we briefly describe the TSH dynamics for the coupled molecule-cavity hybrid system, whereas the details can be found in our previous work.²⁵

We use the fourth-order Runge-Kutta method to integrate the propagation of the quantum subsystem with the Lindblad dynamics, through the EOMs presented in Eq. 27a and Eq. 27b. Specifically, for each nuclear time step, we propagate the quantum subsystem using Eq. 27a and then propagate using Eq. 27b. The classical subsystem (nuclear DOF) is propagated using Newton's EOM with the velocity Verlet algorithm. In the TSH dynamics,⁴⁵ the nuclear force comes from *only one* specific polariton state $|\mathcal{E}_I(\mathbf{R}(t))\rangle$ (eigenstate of \hat{V} , see Eq. 17) as follows

$$\mathbf{F} = -\nabla \mathcal{E}_I(\mathbf{R}), \quad (31)$$

where $\mathcal{E}_I(\mathbf{R})$ is the energy of the *active* adiabatic polariton state, and I is the active state index determined with the TSH algorithm, which will be determined at every nuclear propagation step. The nuclear gradient is calculated as

$$\nabla \mathcal{E}_I(\mathbf{R}) = \langle \mathcal{E}_I(\mathbf{R}) | \nabla V | \mathcal{E}_I(\mathbf{R}) \rangle, \quad (32)$$

as the results of the Hellman-Feynman theorem. Assuming the completeness relation $\sum_i |\psi_i\rangle \langle \psi_i| = \hat{I}$ (where $|\psi_i\rangle = |\phi_\alpha(\mathbf{R}), n\rangle$), and inserting it into Eq. 32, we have

$$\begin{aligned} \nabla \mathcal{E}_I &= \sum_{jk} \langle \mathcal{E}_I | \psi_j \rangle \langle \psi_j | \nabla V | \psi_k \rangle \langle \psi_k | \mathcal{E}_I \rangle \\ &= [\mathbf{U}^T [\nabla V] \mathbf{U}]_{II}, \end{aligned} \quad (33)$$

where the transformation matrix \mathbf{U} can be obtained through Eq. 19, the matrix element of ∇V is expressed as²⁵

$$[\nabla V] \equiv \nabla [V] - [V][\mathbf{d}] + [\mathbf{d}][V], \quad (34)$$

where $[V]$ and $[\mathbf{d}]$ are the matrix of \hat{V} and derivative coupling operator in the adiabatic-Fock state basis and can be calculated with Eq. 11 and Eq. 29, respectively. The detailed derivation of the expression of $[\nabla V]$ (Eq. 34) can be found in Ref. 25.

To evaluate $\nabla [V]$, one needs to take the derivative on each term of V expressed in Eq. 11, including $\nabla E_\nu(\mathbf{R})$ and $\nabla(\epsilon \cdot \boldsymbol{\mu}_{\gamma \nu}(\mathbf{R}))$. The first term is the gradient of the adiabatic electronic state energy, which can be obtained from the *ab initio* electronic structure calculation. The second term can be further expanded using Eq. 16 as

$$\begin{aligned} \nabla(\epsilon \cdot \boldsymbol{\mu}_{\gamma \nu}(\mathbf{R})) &= \nabla(\epsilon_x \mu_{\gamma \nu}^x(\mathbf{R}) + \epsilon_y \mu_{\gamma \nu}^y(\mathbf{R}) + \epsilon_z \mu_{\gamma \nu}^z(\mathbf{R})) \\ &= \epsilon_x \nabla \mu_{\gamma \nu}^x(\mathbf{R}) + \epsilon_y \nabla \mu_{\gamma \nu}^y(\mathbf{R}) + \epsilon_z \nabla \mu_{\gamma \nu}^z(\mathbf{R}), \end{aligned} \quad (35)$$

where one needs to calculate the derivatives of the dipole matrix elements $\nabla \mu_{\gamma \nu}^l(\mathbf{R})$ for $l = x, y, z$. Unfortunately, these derivatives are not implemented for most of the electronic structure methods. We address this theoretical challenge using a machine learning model based on the Kernel ridge regression (KRR) method in this work, which will be extensively discussed in Sec. 2.4.

To further obtain the switching probability of the molecular system from one polariton state to another polariton state, we follow the recently developed global flux surface hopping (GFSH) algorithm.⁴⁷ This algorithm is shown to outperform the original fewest switches algorithm⁴⁵ for systems with more than two electronic states. Here, we briefly describe how to apply it to polaritonic systems. First, we express the density matrix element in the *polariton basis* as follows

$$\rho_{IJ}^{\text{pl}}(t) = c_I(t) c_J^*(t), \quad (36)$$

where $c_I(t)$ is the expansion coefficient of the total wavefunction of the quantum subsystem in the polaritonic basis as

$$|\Psi(\mathbf{r}; \mathbf{R}(t))\rangle = \sum_I c_I(t) |\mathcal{E}_I(\mathbf{R}(t))\rangle. \quad (37)$$

For clarity, we denote the reduced density matrix in the adiabatic-Fock basis as $\rho_{ij}^{\text{af}}(t)$, and $\rho_{IJ}^{\text{pl}}(t)$ is the reduced density matrix in the polariton basis (expressed in Eq. 36). To obtain the density matrix in the polaritonic basis during the dynamics, we use the following unitary transformation

$$[\rho^{\text{pl}}(\mathbf{R}(t))] = \mathbf{U}^\dagger [\rho^{\text{af}}(\mathbf{R}(t))] \mathbf{U}. \quad (38)$$

We employ the GFSH algorithm⁴⁷ to calculate the probability of switching from the active polariton state $|\mathcal{E}_I\rangle$ to *any other* polariton state $|\mathcal{E}_J\rangle$ during the time inter-

val between t and $t + \delta t$ as

$$f_{IJ} = \frac{\Delta\rho_{JJ}^{\text{pl}}}{\rho_{II}^{\text{pl}}} \frac{\Delta\rho_{II}^{\text{pl}}}{\sum_{k \in A} \Delta\rho_{kk}^{\text{pl}}} \quad (\text{if } I \in A \text{ and } J \in B), \quad (39)$$

where $\Delta\rho_{II}^{\text{pl}} = \rho_{II}^{\text{pl}}(t + \delta t) - \rho_{II}^{\text{pl}}(t)$. From time t to $t + \delta t$, all the polariton states that lose population form group A , while all the polariton states that gain population form group B . Here we only need to calculate the switching probability when the current active state $|\mathcal{E}_I\rangle$ belongs to A , and the destination state belongs to B . All other types of state switches, for example, $|\mathcal{E}_I\rangle$ and $|\mathcal{E}_J\rangle$ belong to the same subgroup, or $|\mathcal{E}_I\rangle$ belong to B and $|\mathcal{E}_J\rangle$ belongs to A , are not allowed, and the switching probabilities are set to 0 based on the algorithm.⁴⁷ The non-adiabatic transition, *i.e.* stochastic switches from the currently occupied state $|\mathcal{E}_I\rangle$ to another state $|\mathcal{E}_K\rangle$, occurs if the following condition is satisfied

$$\sum_{J=1}^K f_{IJ} < \zeta < \sum_{J=1}^{K+1} f_{IJ}, \quad (40)$$

where ζ is a uniform randomly generated number between 0 and 1 at each nuclear time step. If the transition is accepted, the active state is set to the new adiabatic state $|\mathcal{E}_K\rangle$.

For each nuclear time step, the density of the quantum subsystem is propagated using Eq. 27a and Eq. 27b. We have to calculate the hopping probabilities and assess if the system should hop to another state for both of these two steps. If a hopping event happens from current state $|\mathcal{E}_I\rangle$ to new $|\mathcal{E}_K\rangle$ due to quantum subsystem evolution itself governed by Eq. 27a, the velocities of the nuclei are re-scaled along the direction of the NAC $\mathbf{d}_{IK}(\mathbf{R})$ in order to conserve the total energy.⁴⁶ In particular, the NAC between two polaritonic states can be expressed as⁴⁶

$$\mathbf{d}_{IJ} = \langle \mathcal{E}_I | \nabla | \mathcal{E}_J \rangle = \frac{\langle \mathcal{E}_I | \nabla V | \mathcal{E}_J \rangle}{\mathcal{E}_J - \mathcal{E}_I}. \quad (41)$$

Note that this should not be confused with the molecular derivative coupling \mathbf{d}_{ij} defined in Eq. 28. One can further express Eq. 41 by inserting the completeness relation as

$$\mathbf{d}_{IJ} = \sum_{jk} \frac{\langle \mathcal{E}_I | \psi_j \rangle \langle \psi_j | \nabla V | \psi_k \rangle \langle \psi_k | \mathcal{E}_J \rangle}{\mathcal{E}_J - \mathcal{E}_I} \quad (42)$$

This NAC in the polariton representation (Eq. 42) is only used for computing the direction of re-scaling the velocity. Further, since the energy of the entire hybrid system is dissipated to the photonic environment during the cavity loss process, there is no energy conservation for the cavity loss process, and as such, we do not perform the velocity scaling for nuclear DOFs if the hopping occurs during the cavity loss process governed by Eq. 27b. This is consistent with the previous work of TSH dynamics in simulating polariton dynamics.^{13,15,27}

In the TSH simulation used in this work, we set one of the polariton states as the initial active state, which means the initial coefficients $c_I(0)$ for the state $|\mathcal{E}_I\rangle$ is set to be one, and the rest of the coefficients are set to be zero. These coefficients $\{c_J(0)\}$ in the polariton state basis can be unitary-transformed into the coefficients $\{c_i(0)\}$ in the adiabatic-Fock state basis to perform the Lindblad dynamics for each nuclear initial condition.

When computing the population dynamics in a representation that is *not* the adiabatic states of $\hat{V} = \hat{H}_{\text{pl}}$, there is no unique way to calculate them in the TSH approach.⁴⁸ In this work, we follow the estimator proposed by Subotnik *et al.*⁴⁸ which shows more accurate results in our previous work for polariton dynamics.²⁶ Below, we briefly introduce this estimator.

To get the adiabatic-Fock state population of the $|\psi_i\rangle$ state ρ_{ii}^{af} from the TSH simulation, the most straightforward way is through following unitary transformation

$$[\rho^{\text{af}}(\mathbf{R}_l(t))] = \mathbf{U}[\rho^{\text{pl}}(\mathbf{R}_l(t))] \mathbf{U}^\dagger, \quad (43)$$

where $[\rho^{\text{pl}}(\mathbf{R}_l(t))]$ is the reduced density matrix in the polariton basis along a given nuclear trajectory $\mathbf{R}_l(t)$, with l as the label of the trajectory. Further, $\mathbf{U}(\mathbf{R}_l(t))$ is the matrix that diagonalize the matrix $[V(\mathbf{R}_l(t))]$ as shown in Eq. 19, along the same trajectory $\mathbf{R}_l(t)$. The adiabatic-Fock state population is then obtained from trajectory average as follows

$$P_i(t) = \frac{1}{N} \sum_l^N [\mathbf{U}[\rho^{\text{pl}}(\mathbf{R}_l(t))] \mathbf{U}^\dagger]_{ii}, \quad (44)$$

where N is the total number of trajectories. Instead of calculating the polaritonic state density matrix $[\rho^{\text{pl}}(\mathbf{R}_l(t))]$ using Eq. 36 directly, in the estimator used in this work, we calculate the diagonal elements of ρ^{pl} using the active state index, and calculate the off-diagonal elements using the polaritonic state expansion coefficients $\{c_I(t)\}$

$$\rho_{IJ}^{\text{pl}}(\mathbf{R}_l(t)) = \begin{cases} \delta_{IK}, & I = J \\ c_I c_J^*, & I \neq J, \end{cases} \quad (45)$$

where K is the active polaritonic state. This estimator was developed in connection with the mixed quantum-classical Liouville equation,⁴⁸ and has shown to provide more accurate diabatic population,⁴⁸ as well as adiabatic-Fock states populations for a Shin-Metiu model coupled to the cavity.²⁶ For the population dynamics of the polariton states $|\mathcal{E}_I(\mathbf{R})\rangle$, we use the traditional active estimator, which is

$$P_I(t) = \frac{1}{N} \sum_l^N \rho_{II}^{\text{pl}}(\mathbf{R}_l(t)). \quad (46)$$

We have also reported the *trans* isomer population, com-

puted as

$$P_{\text{tr}}(t) = \frac{1}{N} \sum_l^N \Theta(|\phi(\mathbf{R}_l(t))| - |\phi_0|), \quad (47)$$

where Θ is the Heaviside function, $|\phi(\mathbf{R}_l(t))|$ is absolute value of the CNNC dihedral angle along the \mathbf{R}_l trajectory, and $|\phi_0| = 90^\circ$ is the dividing surface that distinguishes *cis* and *trans* isomer. The details of polariton dynamics with the TSH method can also be found in our previous work performing QED dynamics with the MQC methods.^{25,26}

2.4 Kernel Ridge Regression Model for Dipoles

As pointed out in Sec. 2.3, the dipoles, including the permanent dipoles and transition dipoles, and their derivatives are necessary ingredients to perform polariton dynamics simulations. However, for realistic molecular systems, the derivatives of dipoles are not readily available for most of the commonly-used excited-state electronic structure methods, such as CASSCF and TD-DFT. Therefore, we circumvent this technical difficulty by employing the *machine learning* techniques in this work to get the *analytical expressions* of dipoles in terms of the molecular geometry $\mu(\mathbf{R}) = f(\mathbf{R})$. After that, we have full access to the analytical expression of derivatives of dipoles using $\nabla\mu(\mathbf{R}) = \nabla f(\mathbf{R})$. Below, we will briefly discuss the machine learning strategy we used to parametrize dipoles, and the details can be found in the previous work on performing on-the-fly non-adiabatic dynamics with the machine-learned potential energy surfaces (PESs).⁴⁹

To obtain the relation between the dipoles and the molecular geometry, we first need to define a proper molecular descriptor to represent the molecular geometry. One simple molecular descriptor is the Coulomb matrix⁵⁰ \mathbf{M} , with the matrix elements defined as follows

$$\mathbf{M}_{kl} = \begin{cases} 0.5Z_k^{2.4} & k = l \\ \frac{Z_k Z_l}{\sqrt{(x_k - x_l)^2 + (y_k - y_l)^2 + (z_k - z_l)^2}} & k \neq l \end{cases}, \quad (48)$$

where Z_k is the atomic number of atom k , (x_k, y_k, z_k) is the Cartesian coordinates of atom k . Note that the diagonal elements of the Coulomb matrix are not dependent on molecular configuration, and thus it is safe to remove them in the construction of molecular descriptor. In addition, the Coulomb matrix is symmetric, thus we only need to consider the off-diagonal elements of the upper triangle part. All of these used off-diagonal elements define a vector \mathbf{m} that contains $N_a \times (N_a - 1)/2$ elements (where N_a is the number of atoms of a single molecule) and are used as input in the training and prediction process. The Coulomb matrix provides a simple and effective representation of molecular geometry, which takes both element types and internal distances

into account and has shown great advantages in building machine learning models as demonstrated in the previous work.^{31,49–52}

In this work, we employ the KRR method in the machine learning process. KRR is one of the most popular *supervised* learning approaches and has been used for the prediction of molecular properties in several studies.^{49,50,53} In the KRR approach, the molecular property $f(\mathbf{m})$, such as the molecular dipole considered in this work, is estimated by a function of the nuclear configurations represented by the molecular descriptor \mathbf{m} . The model assumes that the property can be calculated as the follows

$$f(\mathbf{m}) = \sum_{j=1}^{N_t} w_j K(\mathbf{m}, \mathbf{m}^{(j)}), \quad (49)$$

where $\mathbf{m}^{(j)}$ is the molecular descriptor for the j -th configuration and N_t is the number of configurations in the training dataset, w_j is the regression coefficients. Further, K is the kernel function. In this work, we use the radial basis function (RBF) kernel in the learning algorithms. The RBF kernel is often called the Gaussian kernel, defined as follows

$$K(\mathbf{m}, \mathbf{m}^{(j)}) = \exp\left(-\frac{|\mathbf{m} - \mathbf{m}^{(j)}|^2}{2\sigma^2}\right), \quad (50)$$

where σ is the kernel width, $\mathbf{m} - \mathbf{m}^{(j)}$ is the Euclidean distance between the two molecular descriptor vectors \mathbf{m} and $\mathbf{m}^{(j)}$. The regression coefficients w_j are trained by minimizing the following expression

$$\sum_{i=1}^{N_t} \left[f(\mathbf{m}^{(i)}) - f^{\text{ref}}(\mathbf{m}^{(i)}) \right]^2 + \lambda \mathbf{W}^T \mathbf{K} \mathbf{W}, \quad (51)$$

where f^{ref} is the reference molecular property value. The kernel matrix \mathbf{K} is obtained by Eq. 50 over all pairwise distances between all training data, and λ is a regularization parameter used to prevent over-fitting. After we obtain the regression coefficients w_j , the molecular property $f(\mathbf{m})$ is calculated using Eq. 49.

The first-order derivative of $f(\mathbf{m})$ with respect to Cartesian coordinates (x_k, y_k, z_k) of atom k can be then calculated by the chain rule

$$\frac{\partial f(\mathbf{m})}{\partial l_k} = \sum_s \frac{\partial f(\mathbf{m})}{\partial m_s} \frac{\partial m_s}{\partial l_k}, \quad (52)$$

where $l = x, y, z$, and m_s is an element of \mathbf{m} .

During the training and prediction of the dipoles and their derivatives process, the Coulomb matrix is used as the molecular descriptor, which is invariant to the translational and rotational motion of molecules. However, the dipoles of the molecular system are vectors and will change if we rotate the molecule. Therefore, we define a relative Cartesian coordinate system in this

work, which is dependent on the relative positions between the atoms of the molecule. The dipoles used in the training and prediction process are based on the relative Cartesian coordinate system, which will also be invariant to the translational and rotational motion of molecules. The details of this implementation can be found in the Supporting Information.

3 Computational Details

3.1 Electronic Structure Calculation

The ground-state minima of the two isomers (*cis* and *trans*) of the azomethane molecule were optimized using the DFT method with the B3LYP functional. The frequency analysis was performed to confirm these minima are stationary. The vibrational frequencies were further used in the Wigner sampling process. The CASSCF method^{54,55} was used to obtain the adiabatic energies, gradients, dipoles (permanent and transition dipoles), and NAC of the azomethane molecule in the electronic structure calculations. Following the previous studies,^{39–41} two state average with an active space of six electrons in four orbitals [SA-2-CAS(6,4)] was used in the CASSCF calculations. In all electronic structure calculations, the 6-31G* basis set was used. The DFT and CASSCF calculations were performed using the Gaussian 16⁵⁶ and Molpro 2015⁵⁷ packages, respectively.

It is reported that the conical intersection (CI) between the $|g\rangle$ and $|e\rangle$ states plays an important role in the photoisomerization process of the azomethane molecule.^{39,40} Thus, we optimized the molecular geometry of the CI between the ground state and the first excited state (see the inset geometry with “CI” label in Fig. 1a) using geometry optimization method proposed by Yarkony and co-worker,⁵⁸ as implemented in the Molpro 2015⁵⁷ package. The CI-optimized geometry is obtained at the SA-2-CAS(6,4) level of theory. We also obtained the optimized geometries of both *cis* and *trans* isomers in the ground electronic state, at the level of DFT using B3LYP/6-31G*. The entire isomerization reaction path was generated by linear interpolation in internal coordinates from the CI geometry to both the *cis* isomer and the *trans* isomer. We generated a total of 60 of the geometries along the reaction path, and they are not further optimized (as such, they are just rigid interpolation away from the CI point to the *cis* and *trans* isomers). These geometries are used to plot the PESs in Fig. 1a, as well as used for visualizing the molecular dipoles in Fig. 2, and for polariton PESs and gradients in Fig. 3.

3.2 Training Procedure of the Machine Learning Model

In this work, we employed the KRR method to train the analytical expression of dipoles (permanent and transition dipoles) for the azomethane molecule. All of the training data are generated at the SA-2-CAS(6,4) level of theory, with the 6-31G* basis set. This ensures the dipole and its derivative of it are also at the level of CASSCF, which will be consistent with the other nuclear gradient (see Eq. 34) used in the dynamics simulations. Below, we briefly describe our training procedure.

First, we generated a number of initial conditions (nuclear coordinates and momenta) near the ground-state minimum of the *cis* isomer using the Wigner sampling at T=0 K. Based on these initial conditions, we performed the on-the-fly Born-Oppenheimer molecular dynamics (BOMD) simulations at the $|g\rangle$ and $|e\rangle$ surfaces with 100 and 200 trajectories, respectively. The nuclear motions are propagated using the velocity-Verlet algorithm with a time step of $dt = 0.5$ fs. A total of 30 nuclear steps were run for the dynamics at the $|g\rangle$ state and 700 nuclear steps were run for dynamics at the $|e\rangle$ state. To enhance the sampling of the distribution of the geometries in the dynamics process, we further generate another 200 initial conditions using the Wigner sampling at $T = 1000$ K and performed the BOMD simulations at the $|e\rangle$ state. A total of 100 nuclear propagation steps are run for each trajectory. We performed the same initial sampling and dynamics for the *trans* isomer. In addition, we created 200 conformations by rotating the central NN double bond from the *cis* isomer to the *trans* isomer and performed short-time (30 nuclear steps) BOMD at the $|e\rangle$ state initialized from these conformations.

Second, we collected snapshots of every two nuclear steps (with a time separation of 1 fs) in all the above dynamics to form our dataset library, with a total of 166000 azomethane conformations. We randomly chose 120000 azomethane conformations to build the preliminary training dataset and chose the rest of 46000 configurations to build the testing dataset. As one can see, the training dataset has a huge number of data points. On the one hand, if we used all of these data in the KRR regression, the fitting procedure may become extremely slow and the regression process will require a huge amount of computer memory. On the other hand, in the sampling process, several data points may be located within the same areas, while much fewer points in some other areas. Thus, it is useful to create a balanced description of the data distribution over all important spaces in the regression, as suggested by previous work.^{49,51} The most direct way is to perform the *clustering analysis* of data points before training.

In this work, we took the similarity between the Coulomb matrix of different geometries as the reference to perform clustering with the hierarchical agglomerative clustering algorithm.⁵⁹ The training dataset was

clustered into 1000 groups. Since the data is not well distributed, when we cluster them into subgroups, the number of data in each subgroup varies from each other. The number of data in some subgroups is less than 100, in this case, we selected all the data (geometries) in these subgroups. Otherwise, we selected at most 100 geometries from each group. All selected geometries formed the final training dataset, which contains a total of 72993 azomethane conformations. The wide distribution of the CNNC dihedral angle (see Fig. S2 in the Supporting Information), which is the main reaction coordinate during the isomerization process, indicates that the training dataset is properly sampled in this work.

Finally, we performed the KRR method to fit the machine learning dipoles based on the final training dataset, and then we tested their prediction ability based on the testing dataset. The parameters σ and λ in the training process were set to 0.05 and 0.005 to get the smallest training and test errors. After obtaining the machine-learned dipoles, we get their derivatives using Eq. 52. All the machine learning relevant codes, such as KRR, data prescreening, and the interface with dynamics, were written with the Python language, based on the scikit-learn toolkit.⁶⁰

3.3 Non-adiabatic Polariton Dynamics Simulations

The GFSH approach⁴⁷ was employed in the non-adiabatic dynamics simulations both inside and outside the cavity in this work. The initial condition is generated from a separate (independent) set of initial nuclear configurations near the ground-state minimum of the *cis* isomer using the Wigner sampling at $T = 0$ K. The initial Wigner distribution is sampled from the ground vibrational state $\nu = 0$ on the ground electronic state $|g\rangle$, where the normal mode frequencies (in the harmonic approximation) are calculated based on the approach outlined in Ref. 61,62, as implemented in the JADE-NAMD package.⁶³ In particular, the nuclear density $\rho_W(\tilde{\mathbf{R}}, \tilde{\mathbf{P}})$ in terms of the molecular normal-mode frequencies $\{\tilde{\omega}_k\}$ and phase space variables $\{\tilde{\mathbf{R}}, \tilde{\mathbf{P}}\}$ is given as⁶⁴

$$\rho_W \propto \prod_{k=1}^N \exp \left[-\tanh \left(\frac{\beta \hbar \tilde{\omega}_k}{2} \right) \left(\frac{m \tilde{\omega}_k}{\hbar} \tilde{R}_k^2 + \frac{1}{m_k \tilde{\omega}_k \hbar} \tilde{P}_k^2 \right) \right]. \quad (53)$$

The initial distribution $\{\mathbf{R}, \mathbf{P}\}$ is then obtained by transforming $\{\tilde{\mathbf{R}}, \tilde{\mathbf{P}}\}$ from the normal mode representation to the primitive coordinates using the unitary transformation that diagonalizes the Hessian matrix. All of the initial nuclear geometries for the quantum dynamics simulations are then sampled from the geometries centered at the optimized *cis* isomer (Fig. 2a), which is also used as the reference configuration to de-

fine the global Cartesian system used in this work, see Sec. 4.2 for details. The detailed geometry for each trajectory, of course, fluctuates around the *cis* isomer, governed by the Wigner distribution. As the polariton dynamics proceed, the molecule will move and rotate in space. We do not remove any center of mass translation and rotation during the dynamics simulations.

The trajectories started from the $|e\rangle$ state for dynamics outside the cavity and from the third polaritonic state $|\mathcal{E}_2\rangle$ for the polariton dynamics when coupling the molecule inside the cavity. For all dynamics, the nuclear motion was propagated using the velocity-Verlet algorithm with a time step of $dt = 0.2$ fs. In each nuclear time step, 100 steps are used for the quantum subsystem propagation using Eq. 27a and Eq. 27b. All of the energy, gradient and derivative couplings of the molecules are computed on the fly. All of the population dynamics results are obtained by averaging over 500 trajectories, using the expression of Eq. 44 (for adiabatic-Fock states) and Eq. 46 (for polariton states). The decoherence correction algorithm proposed by Granucci *et al.*⁶⁵ was employed in the GFSH dynamics and the decoherence parameter α was set to 0.1.

Below, we briefly summarize the details of performing the polariton dynamics. First, we use Eq. 53 to generate the initial nuclear condition, including the initial positions and momenta. Then, we use Eq. 27a and Eq. 27b to propagate the quantum dynamics of the electronic-photonic DOFs, while the nuclear DOFs are propagated with force from the active polaritonic state calculated using Eq. 33. In the construction of the system's Hamiltonian and calculation of the nuclear forces, we use the machine learning model to get the dipoles and their derivative using Eq. 49 and Eq. 52, respectively, whereas all of the other quantities, including all energy, gradients, and derivative couplings are computed on-the-fly using CASSCF. During the TSH dynamics, we use Eq. 39 to calculate the hopping probability from a current active state to any other states, and use the Monte Carlo algorithm presented in Eq. 40 to stochastically determine which state the system will hop. Finally, we use Eq. 44 and Eq. 46 to obtain the population of the adiabatic Fock state and polaritonic state, respectively. All the dynamics calculations were performed with a development version of the JADE-NAMD package.^{40,49,63,66,67}

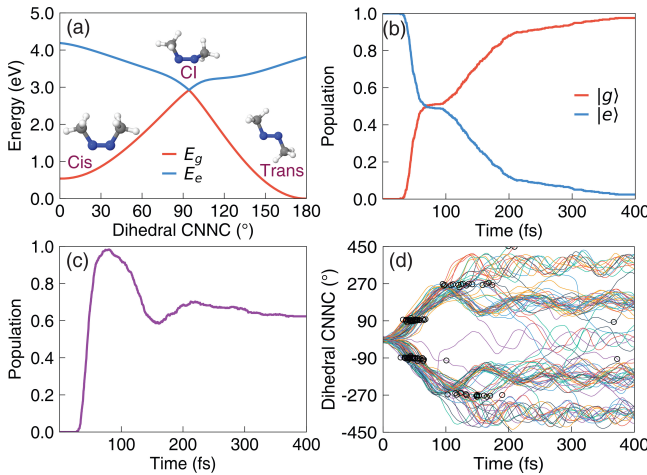


Figure 1: Non-adiabatic dynamics of the azomethane molecule outside the cavity. (a) The potential energy surface of the $|g\rangle$ and $|e\rangle$ states along the reaction pathway (obtained using linear interpolation of the internal coordinates) from the *cis* isomer to the conical intersection configuration and to the *trans* isomer for the azomethane molecule; (b) the electronic population of the $|g\rangle$ and $|e\rangle$ states; (c) the population dynamics of the *trans* isomer; (d) time-dependent value of dihedral CNNC angle (of 100 trajectories), with the black circles indicating where the surface hopping events happen from the $|e\rangle$ state to the $|g\rangle$ state during the trajectory surface hopping simulations.

4 Results and Discussion

4.1 Non-adiabatic Dynamics of the Molecule Outside the Cavity

Fig. 1a presents the electronic adiabatic PESs for $|g\rangle$ (red curve) and $|e\rangle$ (blue curve) along the reaction path, with geometries obtained using procedure described in Sec. 3.1. The inset depicts the molecular structures of azomethane. Two isomers, *cis* and *trans*, exist for this molecule, defined by the CNNC dihedral angle at $\sim 0^\circ$ and $\sim 180^\circ$, respectively. These two isomers can convert to each other upon photoexcitation.⁶⁸ To explore how the photoisomerization process of azomethane can be influenced by the light-matter coupling, we first perform the non-adiabatic dynamics of azomethane *outside* the cavity. Although the *trans* isomer is energetically more stable (with a lower energy of ~ 0.5 eV) than the *cis* isomer in the ground state ($|g\rangle$), we start the dynamics from the *cis* isomer upon a Franck-Condon excitation, due to a larger transition dipole between the ground state ($|g\rangle$) and the first excited state ($|e\rangle$) at the *cis* configuration compared to that of the *trans* isomer.

Fig. 1b presents the time-dependent adiabatic population in the TSH dynamics process. After being excited to the $|e\rangle$ state, the system decays fast and nearly half of the trajectories hop to the $|g\rangle$ state within ~ 50 fs. The fast excited-state population decay process can be explained by the shape of the PES of the $|e\rangle$ state (see

Fig. 1a), where no energy barrier exists along the reaction pathway from the *cis* isomer to the CI. After 50 fs, the decay of the $|e\rangle$ state becomes slower and almost all the trajectories are at the $|g\rangle$ state after ~ 330 fs.

Fig. 1c presents the time-dependent population of the *trans* configuration during the photo-excitation dynamics. In the beginning, all trajectories have the configurations of the *cis* isomer, and thus the *trans* population is zero. This is correlated with the CNNC dihedral angles presented in Fig. 1d, where all trajectories are $\sim 0^\circ$ at $t = 0$. Then the system starts to rotate through the central NN bond and isomerize, with the CNNC dihedral angle passing by 90° or -90° , and the population of *trans* configuration almost increases to one at ~ 70 fs. Many trajectories hop to the ground state in the vicinity of CI, where the CNNC dihedral angles are $\sim 90^\circ$ or $\sim -90^\circ$, as shown in Fig. 1d. The trajectories hop to the ground state and then get trapped in the potential minimum of the *trans* isomer configuration (see Fig. 1a). These trajectories will oscillate around 180° or -180° for the long-time dynamics. Other trajectories will keep rotating, and go back to the *cis* configuration with the CNNC dihedral angles passing by 270° or -270° . Similarly, they are also trapped in the potential minimum of the *cis* isomer and oscillate around 360° or -360° . The rotation from the *trans* isomer back to the *cis* isomer of some trajectories explains why the population in Fig. 1c decreases after ~ 70 fs. The population of *trans* configuration does not change too much after ~ 300 fs, where most of the trajectories are already at the $|g\rangle$ state, as shown in Fig. 1b.

4.2 Machine Learning Model for Dipoles

To perform the non-adiabatic QED simulation with the TSH method, one needs to obtain the molecular dipoles and their derivatives with respect to the nuclear coordinates (see Eq. 11 and Eq. 35). In this work, we use the KRR method to obtain a machine-learning expression of the analytical expression of the dipoles. We then obtain their derivatives using Eq. 52 to compute the contribution of the nuclear gradient due to the derivative of dipoles. As we know, the dipoles of the molecular system, including the permanent dipole and transition dipole, are vectors and have three components in space. Fig. 2a presents the global Cartesian coordinate system defined in this work, which is used to determine the components of dipoles in different directions. For convenience, the optimized geometry of the *cis* isomer is used as the reference geometry (with the XYZ coordinates provided in the Supporting Information). As illustrated in Fig. 2a, the X-axis is defined along the NN bond, the Y-axis is defined as the direction that

is perpendicular to the molecular plane (the plane of the CNNC bond of the *cis* isomer), and the Z-axis is defined perpendicular to the X- and Y-axes simultaneously. Note that the field polarization direction (used in Eq. 7) is also defined in the axis depicted in Fig. 2a. We emphasize that the global Cartesian coordinate system defined in Fig. 2a is a reference coordinate used in the polariton dynamics process, and is different from the relative Cartesian coordinate system, which is only used in the machine learning processes, see Supporting Information for details.

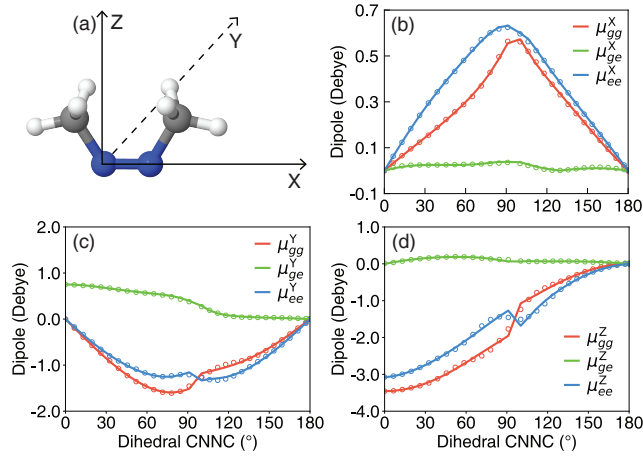


Figure 2: (a) The definition of the global reference Cartesian coordinate system used in this work. The optimized *cis* isomer is used as the reference, where the X-axis is defined along the NN double bond, the Y-axis is defined perpendicular to the molecular plane, and the Z-axis is defined perpendicular to the X- and Y-axes simultaneously. These three directions are also used to define cavity field polarization directions. (b)-(d) The permanent and transition dipole components along the reaction pathway from the *cis* isomer to the conical intersection configuration and to the *trans* isomer, projected along the (b) X direction, (c) Y direction, and (d) Z direction. Results are obtained from the KRR (open circles) and *ab initio* CASSCF calculations (solid lines).

Fig. 2b-d presents the dipoles along the reaction pathway from the *cis* isomer to the *trans* isomer, obtained with the KRR method (open circles) and the CASSCF calculations (solid lines). As one can see, the gradients of these dipoles (slope of the curves in Fig. 2b-d) could get very large, depending on the nuclear configurations, and it is often a drastic approximation to ignore those gradient components in the polariton non-adiabatic simulations. We can see that the machine-learned dipoles consist well with the CASSCF results in all (X, Y, Z) directions. We have also performed additional tests to check the accuracy of our machine-learned dipoles. Fig. S3 in the Supporting Information shows the distribution of the test errors in the learning procedure for the machine-learned dipoles. Note that there are small discrepancies between our machine-

learned model and the actual CASSCF data around the CI configuration (with CNNC angle $\sim 94^\circ$), where the characters of the $|g\rangle$ and $|e\rangle$ states exchange with each other, along with the exchange of their permanent dipoles. There is a “sudden” flip of the permanent dipoles of the $|g\rangle$ and $|e\rangle$ states before and after the CI, which is indicated in the CASSCF-calculated results. However, since the machine-learned dipoles are continuous functions of the nuclear coordinates (Eq. 49), the change of the permanent dipoles obtained with the KRR for each adiabatic electronic state becomes “smooth” around the CI. Considering the NAC between the $|g\rangle$ and $|e\rangle$ states is very large near the CI region and plays a major role when the system arrives at that region in the dynamics process, the discrepancies between the machine-learned dipoles and the CASSCF dipoles near the CI region will not significantly impact to the dynamics inside the cavity, which will be discussed in next sections.

As shown in Fig. 2b-d, the transition dipoles of the *trans* isomer (with CNNC dihedral angle being $\sim 180^\circ$) are zero in all directions due to the symmetry of the *trans* isomer, while the transition dipole of the *cis* isomer has finite value (~ 0.8 Debye) in the Y direction. Hence, the $|e\rangle$ state is a *dark* state at the *trans* configuration, while is a *bright* state at the *cis* configuration. This is also the reason why we chose the *cis* isomer as the initial configuration to perform the dynamics, as mentioned in Sec. 4.1. In addition, we note that near the Franck-Condon region, the permanent dipoles are much smaller than the transition dipole along the Y-axis. In contrast, the permanent dipoles are much larger than the transition dipole along the Z-axis. Moreover, compared to the dipoles along the Y- and Z-axes, the dipoles along the X-axis are much smaller (< 0.7 Debye). As a result, we will only perform the ab-initio molecular cavity QED simulations with the field polarized along the Y- and Z-axes in this work.

In the Supporting Information, we further provide the Polariton PESs obtained from Quantum Optics Models, including the commonly used Jaynes-Cummings model and Quantum Rabi Model. The accuracy and validity of commonly used model systems need to be carefully assessed before adapting them to the field of molecular cavity QED. Unfortunately, these well-established approximations in the atomic cavity QED can explicitly break down in the molecular cavity QED, as shown in Fig. S4-S5. Thus, one needs to use the most rigorous Hamiltonian to describe the light-matter interactions and try to avoid unnecessary approximations. Accordingly, one should use a rigorous QED Hamiltonian (such as Eq. 2) to describe the light-matter interactions and avoid unnecessary approximations.

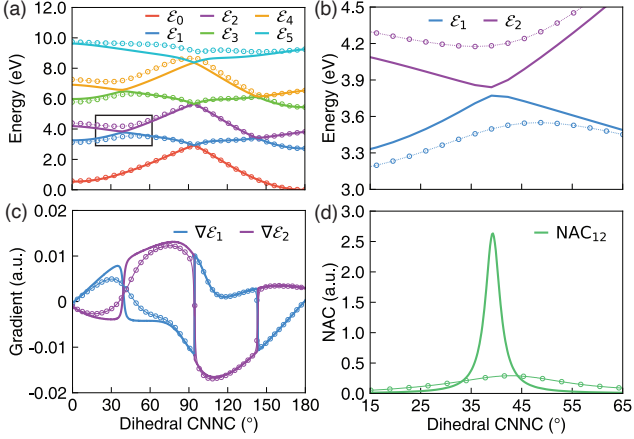


Figure 3: Polariton potentials, gradients, and non-diabatic couplings along the reaction pathway from the *cis* isomer to the conical intersection configuration and to the *trans* isomer for the molecule-cavity hybrid systems. The cavity frequency is set to $\hbar\omega_c = 2.72$ eV. The field is polarized along the Y-axis. The results obtained with the light-matter coupling strength $g_c = 0.005$ a.u. (solid line) and $g_c = 0.05$ a.u. (open circles). (a) Polariton Potential Energy Surface $E_I(R)$. (b) The zoomed-in plot of the Polariton potential of $|\mathcal{E}_1\rangle$ and $|\mathcal{E}_2\rangle$ surfaces. (c) nuclear gradients associated with the $|\mathcal{E}_1\rangle$ and $|\mathcal{E}_2\rangle$ states. (d) Non-adiabatic coupling $\langle \mathcal{E}_1 | \nabla | \mathcal{E}_2 \rangle$ between the two polariton states.

4.3 Ab-initio On-the-fly Polariton Quantum Dynamics

Next, we present the *ab initio* polariton dynamics simulation results obtained using the TSH method described in Sec. 3.3. In this section, the field is polarized along the Y-axis, which means $(\epsilon_x, \epsilon_y, \epsilon_z)$ in Eq. 16 is set to be $(0, 1, 0)$. In this case, only the component of dipoles along the Y-axis will contribute to the polariton dynamics. Two different light-matter coupling strengths $g_c = 0.005$ a.u. and $g_c = 0.05$ a.u., are used here. These light-matter couplings cause the Rabi splitting between the polariton states $|\mathcal{E}_2\rangle$ (commonly referred to as the Upper Polariton state) and $|\mathcal{E}_1\rangle$ (commonly referred to as the Lower Polariton state), with $\hbar\Omega_R = 68$ meV (for $g_c = 0.005$ a.u.) and $\hbar\Omega_R = 680$ meV (for $g_c = 0.05$ a.u.). In our simulations, we will consider a range of cavity loss, with the largest one being $\Gamma = 64$ meV. Note that strong coupling in cavity QED refers to $\hbar\Omega_R \ll \Gamma$ (as well as larger than the molecular excitation decay rate). As such, $g_c = 0.05$ a.u. always satisfies the strong coupling condition and for $g_c = 0.005$ a.u., one needs to consider the cavity loss rate Γ .

Fig. 3a presents the PESs of the polaritonic states (see Eq. 17) along the reaction pathway from the *cis* isomer to the *trans* isomer, with the cavity frequency $\hbar\omega_c = 2.72$ eV. We use two adiabatic electronic states ($|g\rangle$ and $|e\rangle$) and three Fock states ($|0\rangle$, $|1\rangle$ and $|2\rangle$) in the construction of the adiabatic-Fock state basis, which produces six polaritonic states, all of which are included

in the dynamics process. The PESs are obtained with the light-matter coupling strength $g_c = 0.005$ a.u. (depicted in solid lines) and $g_c = 0.05$ a.u. (depicted in open circles). Fig. 3b provides a zoom-up of the square region highlighted in Fig. 3a. An avoided crossing exists between the polaritonic states $|\mathcal{E}_2\rangle$ and $|\mathcal{E}_1\rangle$ due to the light-matter coupling, and the energy gap (so-called the Rabi splitting) increases along with the increase of the coupling strength. Fig. 3c presents the nuclear gradients at the $|\mathcal{E}_1\rangle$ and $|\mathcal{E}_2\rangle$ states, and Fig. 3d presents NAC between them along the reaction pathway. The one-dimension gradients and NAC for each geometry along the reaction pathway are obtained by projecting the gradients and NACs in the whole space (including all nuclear DOFs) to the vector defined by the difference between the Cartesian coordinates of geometries before and after the current geometry. The gradients consist well with the change of the PESs (Fig. 3a), and the NAC between the $|\mathcal{E}_1\rangle$ and $|\mathcal{E}_2\rangle$ states decreases when the light-matter coupling strength increases as expected.

Fig. 4 presents the results of our *ab initio* polariton quantum dynamics simulation, using the CASSCF *ab initio* calculation for all quantities, except for dipoles and their derivatives which are obtained from the machine learning model trained at the CASSCF level. Fig. 4a presents the population dynamics of the polaritonic states, with the light-matter coupling strength $g_c = 0.005$ a.u. (depicted in solid lines) and $g_c = 0.05$ a.u. (depicted in open circles). When the light-matter coupling is relatively small (with coupling strength $g_c = 0.005$ a.u.), the initial polariton population in $|\mathcal{E}_2\rangle$ decays very fast to the $|\mathcal{E}_1\rangle$ state in the first 60 fs of the dynamics. The population of the $|\mathcal{E}_0\rangle$ state begins to grow at ~ 30 fs, and nearly all trajectories have hopped to the $|\mathcal{E}_0\rangle$ state at the end of the dynamics. Other high-lying excited states, like $|\mathcal{E}_3\rangle$, $|\mathcal{E}_4\rangle$, $|\mathcal{E}_5\rangle$ are barely populated during the polariton dynamics process. Besides the polaritonic populations, we can also understand the population dynamics in the adiabatic-Fock states, as shown in Fig. 4b. Since the light-matter coupling is weak when $g_c = 0.005$ a.u. (depicted in solid lines), the $|\mathcal{E}_2\rangle$ state near the Franck-Condon region is mostly composed of the $|e0\rangle$ state. Thus, the population of the $|e0\rangle$ state is nearly one at the beginning of the dynamics. Then, the population transfers to the $|g0\rangle$ state due to the electronic NAC between $|e\rangle$ and $|g\rangle$ states. During this process, we can see a small population of the $|g1\rangle$ state, which is induced by the light-matter coupling dominated by the transition dipole between $|e\rangle$ and $|g\rangle$.

When the light-matter coupling strength is increased to $g_c = 0.05$ a.u., the results are plotted with open circles in Fig. 4. First, the transition process of the system from the $|\mathcal{E}_2\rangle$ state to the $|\mathcal{E}_1\rangle$ state slows down (Fig. 4a) due to the decrease of the NAC between the $|\mathcal{E}_2\rangle$ and $|\mathcal{E}_1\rangle$ states (Fig. 3d). The decay process of the system to the $|\mathcal{E}_0\rangle$ is also postponed, see Fig. 4a. Second, the population of $|g1\rangle$ state is largely increased due to the increase of the light-matter coupling strength, as

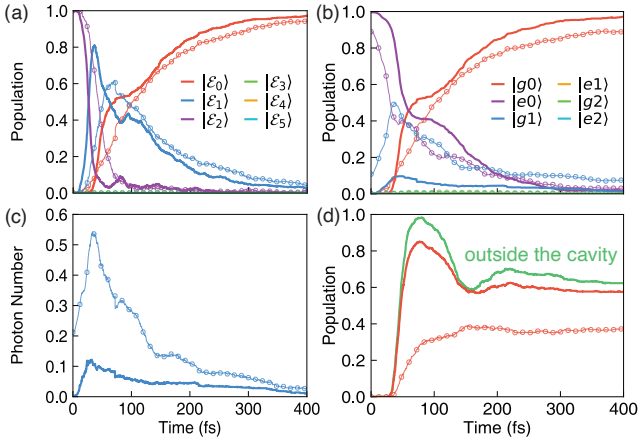


Figure 4: The time-dependent properties obtained from the *ab initio* on-the-fly molecular cavity QED simulations. The cavity loss rate is set to $\Gamma = 4$ meV. The field is polarized along the Y-axis. The cavity frequency is set to $\hbar\omega_c = 2.72$ eV. The results obtained with the light-matter coupling strength $g_c = 0.005$ a.u. (solid lines) and $g_c = 0.05$ a.u. (open circles). (a) population of the Polaritonic states (see Eq. 18); (b) population of the adiabatic-Fock states (see Eq. 10); (c) the average photon number population inside the cavity; (d) population of the *trans* isomer outside the cavity (green solid) and inside the cavity (red curves), with $g_c = 0.005$ a.u. (red solid line) and $g_c = 0.05$ a.u. (red open circles).

shown in Fig. 4b.

Fig. 4c presents the number of photons during the dynamics process. Note that $\hat{a}^\dagger \hat{a}$ is not the “photon number” operator under the dipole gauge used in the PF Hamiltonian^{69,70} because the rigorous photon number operator should be obtained by applying the Power-Zienau-Woolley (PZW) Gauge transformation^{71–73} on the photon number operator $\hat{a}^\dagger \hat{a}$. The correct photon number operator under the dipole gauge is

$$\hat{N} = \frac{1}{\hbar\omega_c}(\hat{H}_p + \hat{H}_{\text{enp}} + \hat{H}_d) - \frac{1}{2} = \hat{a}^\dagger \hat{a} + \frac{1}{\hbar\omega_c}(\hat{H}_{\text{enp}} + \hat{H}_d).$$

The time-dependent photonic population is then computed as $\langle \Psi(t) | \hat{N} | \Psi(t) \rangle = \text{Tr}[\hat{\rho}(t)\hat{N}] = \sum_{ij} \rho_{ij}(t) \langle \psi_j | \hat{N} | \psi_i \rangle$, with the polariton wavefunction $|\Psi(t)\rangle$ expressed in Eq. 25, and reduced density $\rho_{ij}(t)$ in Eq. 26. Since most of the photonic character is contributed from the $|g1\rangle$ state, the evolution of the photon number is very similar to that of the population of the $|g1\rangle$ state as shown in Fig. 4b. For a larger light-matter coupling strength ($g_c = 0.05$ a.u.), because of a larger population for $|g1\rangle$ state (Fig. 4b), the resulting photon number inside the cavity is also larger.

Fig. 4d presents the time-dependent population of the *trans* configurations when coupling the molecule to the cavity. In particular, we compare the case of the *trans* population dynamics outside the cavity (green solid line) with the case of coupling the molecule inside the cavity, with the coupling strength of $g_c = 0.005$

a.u. (red solid lines) and $g_c = 0.05$ a.u. (red open circles). We have observed a significant suppression of the trans population when the molecule is strongly coupled to the cavity. As such, this simulation demonstrates the suppression of the isomerization reaction from *cis*-to-*trans* configuration, when considering realistic cavity loss. The reason for the suppression of the *cis*-to-*trans* reaction is that more trajectories are staying on the $|\mathcal{E}_2\rangle$ state after leaving the Franck-Condon region due to the decrease of the *polaritonic* NAC between the $|\mathcal{E}_2\rangle$ state and $|\mathcal{E}_1\rangle$ state, as clearly shown in Fig. 3d. The above results clearly demonstrate that the chemical reaction of the molecular system can be controlled by the light-matter coupling, and even effectively controlled by tuning the light-matter coupling strength, agreeing with what we have observed in our previous work using a simple model system.⁶

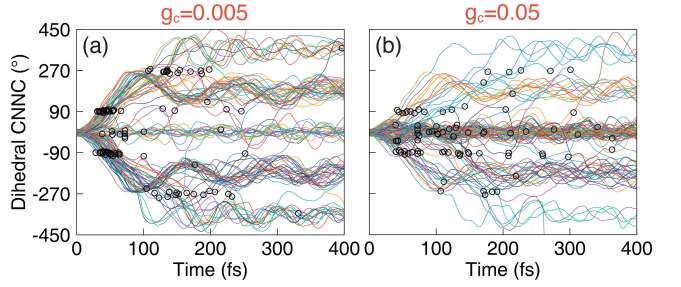


Figure 5: The time-dependent CNNC dihedral angles of 100 trajectories generated from the QED simulations of the azomethane molecule coupled to the cavity, with light-matter coupling strength (a) $g_c = 0.005$ a.u. and (b) $g_c = 0.05$ a.u. The cavity loss rate is set to $\Gamma = 4$ meV. The field is polarized along the Y-axis. The cavity frequency is set to $\hbar\omega_c = 2.72$ eV. The black circles indicate where the surface hopping events happen from the $|\mathcal{E}_1\rangle$ state to the $|\mathcal{E}_0\rangle$ state during the trajectory surface hopping simulations.

Fig. 5a presents the CNNC dihedral angles during the dynamics process to illustrate how light-matter interactions affect the reaction ratio of the azomethane molecule, with the light-matter coupling strength $g_c = 0.005$ a.u. In this figure, we print out the event of the hopping between $|\mathcal{E}_1\rangle$ polariton state to $|\mathcal{E}_0\rangle$ polariton state. Here, we randomly selected 100 trajectories out of the 500 trajectories we generated in the simulation. As opposed to the case of outside the cavity (Fig. 1d) where essentially no trajectory appears around the 0° CNNC dihedral angle, when coupling to the cavity, more trajectories are trapped around the *cis* isomer (Fig. 5a) located at the 0° CNNC dihedral angle, and the CNNC dihedral angles of these trajectories oscillate centered at 0° . This indicates that fewer trajectories will go to the *trans* configuration, resulting in the suppression of the reaction ratio inside the cavity. Fig. 5b presents the same results with a stronger light-matter coupling strength $g_c = 0.05$ a.u., where the fraction of trajectories trapped in the *cis* configuration region is further

enhanced. The reason for the restricted motion of these trajectories is clear. After the trajectory leaves the Franck-Condon region, a large fraction of trajectories will evolve on the $|\mathcal{E}_2\rangle$ state, as opposed to all moving to the electronic conical intersection between $|e\rangle$ and $|g\rangle$. Note that although the NAC between the $|\mathcal{E}_2\rangle$ state and $|\mathcal{E}_1\rangle$ state is large (Fig. 3d), not all trajectories will hop to the $|\mathcal{E}_1\rangle$ state immediately when they approach the avoided crossing region between the $|\mathcal{E}_2\rangle$ and $|\mathcal{E}_1\rangle$ state. As shown in Fig. 3a, there is a large energy barrier on the $|\mathcal{E}_2\rangle$ polariton surface (violet curve), with the peak of the potential barrier located at the CNNC dihedral angle $\sim 90^\circ$ (because it is largely the $|g_1\rangle$ state in that region). Hence, the rotation of these trajectories on the $|\mathcal{E}_2\rangle$ surfaces from *cis* to the *trans* configuration will be suppressed, and these trajectories are eventually forced back to the *cis* configuration region on the $|\mathcal{E}_2\rangle$ surface. These trajectories will pass by the $|\mathcal{E}_2\rangle$ and $|\mathcal{E}_1\rangle$ avoided crossing region again and either hop to the $|\mathcal{E}_1\rangle$ state or stay on the $|\mathcal{E}_2\rangle$ surface. Eventually, they will decay to the $|\mathcal{E}_0\rangle$ state around the *cis* isomer due to the cavity loss, giving rise to the hopping event indicated as the open circles in Fig. 5. Note that there are many number of hops between $|\mathcal{E}_2\rangle$ and $|\mathcal{E}_1\rangle$ surfaces as well. For clarity, we have not indicated these hopping events in the current plot.

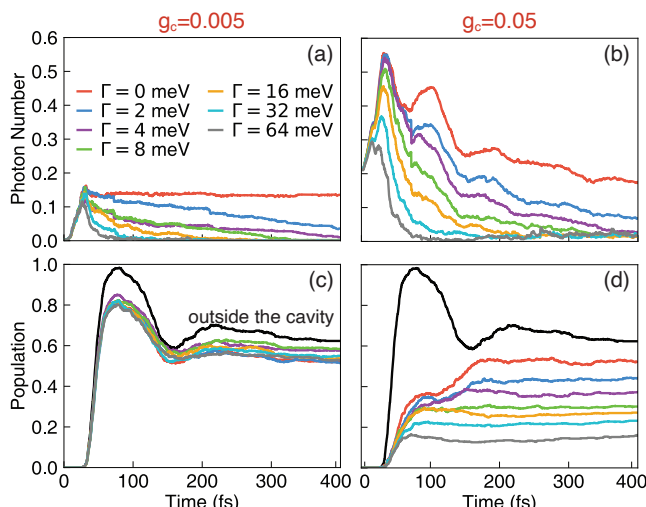


Figure 6: Polariton dynamics with changing cavity loss rate Γ . (a)-(b) The time-dependent photon number dynamics, and (c)-(d) population of the *trans* isomer in the QED simulation with various cavity loss rates Γ . The light-matter coupling strengths are $g_c = 0.005$ a.u. (in (a) and (c)) and $g_c = 0.05$ a.u. (in (b) and (d)), respectively. The field is polarized along the Y-axis. The cavity frequency is set to $\hbar\omega_c = 2.72$ eV. The black lines in panels (c) and (d) are the results outside the cavity, whereas the results inside the cavity with various Γ are color-coded using the legend inside panel (a).

Fig. 6 presents the influence of the cavity loss rate Γ on average photon numbers (panels a-b) as well as the population of the trans isomer (panels c-d), with two

different light-matter coupling strength $g_c = 0.005$ a.u. (left column) and $g_c = 0.05$ a.u. (right column). For realistic molecule-cavity hybrid systems, due to the interaction between the cavity mode and the far-field photon modes outside the cavity, the lifetime of the cavity is always finite. In this work, we use the Lindblad dynamics to incorporate cavity loss in the TSH dynamics. To investigate how cavity loss can impact the chemical reaction, we perform the dynamics inside the cavity with different cavity loss rates Γ . For two coupling cases where $g_c = 0.005$ a.u. and $g_c = 0.05$ a.u. the average photon number decrease when the cavity loss rate Γ increases, as clearly shown in Fig. 6a and b.

Moreover, when the cavity loss rate increases, the magnitude of modification of the reaction ratio inside the cavity also decreased, as shown in Fig. 6c-d. This is more clear for a reasonably large coupling strength $g_c = 0.05$ a.u. Normally, one would expect that when the loss rate is much larger than the Rabi splitting, the hybrid system will go back to the weak coupling regime and one will no longer observe the Rabi splitting from spectroscopy measurements. For the reactivities of the molecule, one can also see an enhanced suppression of the forward reaction from the *cis* to the *trans* isomer. This is because the $|\mathcal{E}_1\rangle$ exciton state very quickly decays to the ground polariton states, thus preventing the isomerization from happening in the excited states. These numerical results could provide theoretical insights into the original Ebbesen experiments on photo-isomerization.⁸ This means that even for a lossy cavity, one can protect the molecule from being isomerized by coupling it to a resonant cavity, resulting in suppressed reactivities. Of course, we emphasize that we are only simulating a single molecule coupled to the cavity, whereas most of the experiments are conducted under the collective coupling regime where a lot of molecules are coupled to the cavity.

5 Conclusion

In this work, we perform the on-the-fly non-adiabatic dynamics simulation of a realistic molecular system coupled to the cavity. We extend the TSH method to simulate the quantum dynamics of coupled electronic-photonic-nuclear DOFs, and use the accurate nuclear gradient expressions developed in our previous work.²⁵ The cavity loss is described with the Lindblad super operator, ensuring proper treatment of both population decay and decoherence among states.²⁸ During the polariton dynamics simulations, the energies and gradients of the electronic states as well as the NAC between them are directly obtained from the *ab initio* one-the-fly electronic structure calculations at the level of CASSCF,

while the molecular dipoles (including permanent and transition dipoles) and their derivatives are obtained from the machine learning model which is also trained with the data at the CASSCF level.

In the construction of the machine learning model of dipoles, we employ the KRR approach and the Coulomb matrix as the molecular descriptor to represent the molecular geometry. We define a relative Cartesian coordinate system (as opposed to the actual Cartesian coordinates of the molecule) in the machine learning process. Similar to the Coulomb matrix, dipoles can also be invariant to the translational and rotational motion of molecules based on the relative Cartesian coordinate system. The relative Cartesian coordinate system defined in this work provides the possibility to fit a molecular property that is dependent on the orientation of the molecular geometry. In the training process, we use the hierarchical agglomerative clustering algorithm, which largely reduces the training dataset as well as the testing error.

We use azomethane as an example to investigate its photoisomerization reaction inside the cavity. We present the non-adiabatic dynamics simulations outside the cavity for comparison. The results show that the machine learning model works well in the prediction of molecular dipoles, and derivatives. In addition, we observe that the reaction ratio of azomethane from the *cis* configuration to *trans* configuration can be well controlled by tuning the light-matter coupling strengths, the polarized directions of the electric field (see additional results in Supporting Information), and the cavity loss rates. We further provide mechanistic insight into how cavity can modify photochemical reactivities by carefully analyzing the population dynamics, cavity loss process, and the time evolution of the key nuclear degrees of freedom, the CNNC dihedral angle. We envision our theoretical results may provide new inspiration for the experimental investigations on polariton photochemistry in the molecule-cavity hybrid system.

The work demonstrates the powerful role of machine learning techniques in the on-the-fly *ab initio* polariton dynamics. By using the machine learning model in this work, if one electronic structure calculation method can provide the molecular dipoles, we can in principle employ it in the polariton dynamics simulations using any MQC methods. This opens the possibility of simulating the polariton dynamics with the excited-state electronic structure calculation methods that can treat more complex molecular systems, such as algebraic diagrammatic construction method to the second order [ADC(2)]^{74,75} or time-dependent density functional theory (TD-DFT).^{76,77} Finally, although only a single molecule and a single cavity mode are considered in this work, we can extend the machine learning model to simulate collective molecules inside the cavity with multiple

cavity modes if we can get all the molecular properties (energies, dipoles, NACs) with machine learning techniques. This will be the future direction of the current work. We envision that the machine learning model for construction dipoles and their derivatives presented in this work will benefit the quantum dynamics community aiming at using *ab initio* simulations to investigate polariton dynamics in realistic molecule-cavity hybrid systems.

Supporting Information

The details of the relative Cartesian coordinate system; the distribution of CNNC dihedral angles in the training dataset; additional data for the test error in the KRR process; the derivation of the photon number operator in the dipole gauge; polariton potential energy surfaces with different Hamiltonian models; additional polariton dynamics results with the field polarized along the Z-axis; Cartesian coordinates for the optimized *cis* isomer, *trans* isomer, and the conical intersection geometries.

Acknowledgement This work was supported by the National Science Foundation CAREER Award under Grant No. CHE-1845747 and by a Cottrell Scholar award (a program by Research Corporation for Science Advancement). Computing resources were provided by the Center for Integrated Research Computing (CIRC) at the University of Rochester. D.H. appreciates valuable discussions with Braden Weight and Eric Koessler.

References

- (1) Ebbesen, T. W. Hybrid Light–Matter States in a Molecular and Material Science Perspective. *Acc. Chem. Res.* **2016**, *49*, 2403–2412.
- (2) Kowalewski, M.; Mukamel, S. Manipulating molecules with quantum light. *Proc. Natl. Acad. Sci. U.S.A.* **2017**, *114*, 3278–3280.
- (3) Flick, J.; Ruggenthaler, M.; Appel, H.; Rubio, A. Atoms and molecules in cavities, from weak to strong coupling in quantum-electrodynamics (QED) chemistry. *Proc. Natl. Acad. Sci. USA* **2017**, *114*, 3026–3034.
- (4) Ribeiro, R. F.; Martínez-Martínez, L. A.; Du, M.; Camos-Gonzalez-Angulo, J.; Yuen-Zhou, J. Polariton chemistry: controlling molecular dynamics with optical cavities. *Chem. Sci.* **2018**, *9*, 6325–6339.

- (5) Feist, J.; Galego, J.; Garcia-Vidal, F. J. Polaritonic chemistry with Organic Molecules. *ACS Photonics* **2018**, *5*, 205–216.
- (6) Mandal, A.; Huo, P. Investigating New Reactivities Enabled by Polariton Photochemistry. *J. Phys. Chem. Lett.* **2019**, *10*, 5519–5529.
- (7) Ruggenthaler, M.; Sidler, D.; Rubio, A. Understanding polaritonic chemistry from ab initio quantum electrodynamics. *arXiv* **2022**,
- (8) Hutchison, J. A.; Schwartz, T.; Genet, C.; Devaux, E.; Ebbesen, T. W. Modifying Chemical Landscapes by Coupling to Vacuum Fields. *Angew. Chem. Int. Ed.* **2012**, *51*, 1592–1596.
- (9) Thomas, A.; Lethuillier-Karl, L.; Nagarajan, K.; Vergauwe, R. M. A.; George, J.; Chervy, T.; Shalabney, A.; Devaux, E.; Genet, C.; Moran, J.; Ebbesen, T. W. Tilting a ground-state reactivity landscape by vibrational strong coupling. *Science* **2019**, *363*, 615–619.
- (10) Mandal, A.; Krauss, T. D.; Huo, P. Polariton-Mediated Electron Transfer via Cavity Quantum Electrodynamics. *J. Phys. Chem. B* **2020**, *124*, 6321–6340.
- (11) Luk, H. L.; Feist, J.; Toppari, J. J.; Groenhof, G. Multiscale Molecular Dynamics Simulations of Polaritonic Chemistry. *J. Chem. Theory Comput.* **2017**, *13*, 4324–4335.
- (12) Groenhof, G.; Toppari, J. J. Coherent Light Harvesting through Strong Coupling to Confined Light. *J. Phys. Chem. Lett.* **2018**, *9*, 4848–4851.
- (13) Fregoni, J.; Granucci, G.; Coccia, E.; Persico, M.; Corni, S. Manipulating azobenzene photoisomerization through strong light-molecule coupling. *Nat. Commun.* **2018**, *9*, 4688.
- (14) Groenhof, G.; Climent, C.; Feist, J.; Morozov, D.; Toppari, J. J. Tracking Polariton Relaxation with Multiscale Molecular Dynamics Simulations. *J. Phys. Chem. Lett.* **2019**, *10*, 5476–5483.
- (15) Fregoni, J.; Corni, S.; Persico, M.; Granucci, G. Photochemistry in the strong coupling regime: A trajectory surface hopping scheme. *J. Comput. Chem.* **2020**, *41*, 2033–2044.
- (16) Tichauer, R. H.; Feist, J.; Groenhof, G. Multiscale dynamics simulations of molecular polaritons: The effect of multiple cavity modes on polariton relaxation. *J. Chem. Phys.* **2021**, *154*, 104112.
- (17) Tichauer, R. H.; Morozov, D.; Sokolovskii, I.; Toppari, J. J.; Groenhof, G. Identifying Vibrations that Control Non-adiabatic Relaxation of Polaritons in Strongly Coupled Molecule–Cavity Systems. *J. Phys. Chem. Lett.* **2022**, *13*, 6259–6267.
- (18) Kowalewski, M.; Bennett, K.; Mukamel, S. Non-adiabatic dynamics of molecules in optical cavities. *J. Chem. Phys.* **2016**, *144*, 054309.
- (19) Lacombe, L.; Hoffmann, N. M.; Maitra, N. T. Exact Potential Energy Surface for Molecules in Cavities. *Phys. Rev. Lett.* **2019**, *123*, 083201.
- (20) Ulusoy, I. S.; Vendrell, O. Dynamics and spectroscopy of molecular ensembles in a lossy microcavity. *J. Chem. Phys.* **2020**, *153*, 044108.
- (21) Lindoy, L. P.; Mandal, A.; Reichman, D. R. Quantum Dynamics of Vibrational Polariton Chemistry. *arXiv* **2022**,
- (22) Zhang, Y.; Nelson, T.; Tretiak, S. Non-adiabatic molecular dynamics of molecules in the presence of strong light-matter interactions. *J. Chem. Phys.* **2019**, *151*, 154109.
- (23) Antoniou, P.; Suchanek, F.; Varner, J. F.; Foley, J. J. Role of Cavity Losses on Nonadiabatic Couplings and Dynamics in Polaritonic Chemistry. *J. Phys. Chem. Lett.* **2020**, *11*, 9063–9069.
- (24) Rosenzweig, B.; Hoffmann, N. M.; Lacombe, L.; Maitra, N. T. Analysis of the classical trajectory treatment of photon dynamics for polaritonic phenomena. *J. Chem. Phys.* **2022**, *156*, 054101.
- (25) Zhou, W.; Hu, D.; Mandal, A.; Huo, P. Nuclear Gradient Expressions for Molecular Cavity Quantum ElectrodynamicsSimulations using Mixed Quantum-Classical Methods. *J. Chem. Phys.* **2022**, *157*, 104118.
- (26) Hu, D.; Mandal, A.; Weight, B. M.; Huo, P. Quasi-Diabatic Propagation Scheme for Simulating Polariton Chemistry. *J. Chem. Phys.* **2022**, *157*, 194109.
- (27) Fregoni, J.; Granucci, G.; Persico, M.; Corni, S. Strong Coupling with Light Enhances the Photoisomerization Quantum Yield of Azobenzene. *Chem* **2020**, *6*, 250–265.
- (28) Koessler, E.; Mandal, A.; Huo, P. Incorporating Lindblad Decay Dynamics into Mixed Quantum-Classical Simulations. *J. Chem. Phys.* **2022**, *157*, 064101.
- (29) Jaynes, E.; Cummings, F. Comparison of Quantum and Semiclassical Radiation Theories with Application to the Beam Maser. *Proc. IEEE* **1963**, *18*, 89–109.

- (30) Ramakrishnan, R.; von Lilienfeld, O. A. *Reviews in Computational Chemistry*; John Wiley & Sons, Ltd, 2017; Chapter 5, pp 225–256.
- (31) Westermayr, J.; Marquetand, P. Machine Learning for Electronically Excited States of Molecules. *Chem. Rev.* **2021**, *121*, 9873–9926.
- (32) Marquetand, P. Recent Progress in Electro- and Photocatalyst Discovery with Machine Learning. *Chem. Rev.* **2022**, *122*, 15996–15997.
- (33) Li, J.; Lopez, S. A. A Look Inside the Black Box of Machine Learning Photodynamics Simulations. *Acc. Chem. Res.* **2022**, *55*, 1972–1984.
- (34) Dral, P. O., Ed. *Quantum Chemistry in the Age of Machine Learning*; Elsevier, 2023.
- (35) Burton, K. A.; Weisman, R. B. Stepwise photodissociation of vapor-phase azomethane. *J. Am. Chem. Soc.* **1990**, *112*, 1804–1807.
- (36) Diau, E. W.; Abou-Zied, O. K.; Scala, A. A.; Ze-wail, A. H. Femtosecond dynamics of transition states and the concept of concertedness: Nitrogen extrusion of azomethane reactions. *J. Am. Chem. Soc.* **1998**, *120*, 3245–3246.
- (37) Cattaneo, P.; Persico, M. Semiclassical Simulations of Azomethane Photochemistry in the Gas Phase and in Solution. *J. Am. Chem. Soc.* **2001**, *123*, 7638–7645.
- (38) Sellner, B.; Ruckenbauer, M.; Stambolić, I.; Barbatti, M.; Aquino, A. J. A.; Lischka, H. Photodynamics of Azomethane: A Nonadiabatic Surface-Hopping Study. *The J. Phys. Chem. A* **2010**, *114*, 8778–8785.
- (39) Gaenko, A.; DeFusco, A.; Varganov, S. A.; Martínez, T. J.; Gordon, M. S. Interfacing the Ab Initio Multiple Spawning Method with Electronic Structure Methods in GAMESS: Photodecay of trans-Azomethane. *The J. Phys. Chem. A* **2014**, *118*, 10902–10908.
- (40) Hu, D.; Xie, Y.; Peng, J.; Lan, Z. On-the-Fly Symmetrical Quasi-Classical Dynamics with Meyer–Miller Mapping Hamiltonian for the Treatment of Nonadiabatic Dynamics at Conical Intersections. *J. Chem. Theory Comput.* **2021**, *17*, 3267–3279.
- (41) Xu, C.; Lin, K.; Hu, D.; Gu, F. L.; Gelin, M. F.; Lan, Z. Ultrafast Internal Conversion Dynamics through the on-the-Fly Simulation of Transient Absorption Pump–Probe Spectra with Different Electronic Structure Methods. *J. Phys. Chem. Lett.* **2022**, *13*, 661–668.
- (42) Flick, J.; Appel, H.; Ruggenthaler, M.; Rubio, A. Cavity Born–Oppenheimer Approximation for Correlated Electron–Nuclear–Photon System. *J. Chem. Theory Comput.* **2017**, *13*, 1616–1625.
- (43) Torres-Sánchez, J.; Feist, J. Molecular photodissociation enabled by ultrafast plasmon decay. *J. Chem. Phys.* **2021**, *154*, 014303.
- (44) Davidsson, E.; Kowalewski, M. Simulating photodissociation reactions in bad cavities with the Lindblad equation. *J. Chem. Phys.* **2020**, *153*, 234304.
- (45) Tully, J. C. Molecular dynamics with Electronic Transitions. *J. Chem. Phys.* **1990**, *93*, 1061–1071.
- (46) Hammes-Schiffer, S.; Tully, J. C. Proton Transfer in Solution: Molecular Dynamics with Quantum Transitions. *J. Chem. Phys.* **1994**, *12*, 4657–4667.
- (47) Wang, L.; Trivedi, D.; Prezhdo, O. V. Global Flux Surface Hopping Approach for Mixed Quantum-Classical Dynamics. *J. Chem. Theory Comput.* **2014**, *10*, 3598–3605.
- (48) Landry, B. R.; Falk, M. J.; Subotnik, J. E. Communication: The correct interpretation of surface hopping trajectories: How to calculate electronic Properties. *J. Chem. Phys.* **2013**, *139*, 211101.
- (49) Hu, D.; Xie, Y.; Li, X.; Li, L.; Lan, Z. Inclusion of machine learning kernel ridge regression potential energy surfaces in on-the-fly nonadiabatic molecular dynamics simulation. *J. Phys. Chem. Lett.* **2018**, *9*, 2725–2732.
- (50) Rupp, M.; Tkatchenko, A.; Müller, K.-R.; Von Lilienfeld, O. A. Fast and accurate modeling of molecular atomization energies with machine learning. *Phys. Rev. Lett.* **2012**, *108*, 058301.
- (51) Häse, F.; Valleau, S.; Pyzer-Knapp, E.; Aspuru-Guzik, A. Machine learning exciton dynamics. *Chem. Sci.* **2016**, *7*, 5139–5147.
- (52) Li, J.; Stein, R.; Adrián, D. M.; Lopez, S. A. Machine-Learning Photodynamics Simulations Uncover the Role of Substituent Effects on the Photochemical Formation of Cubanes. *J. Am. Chem. Soc.* **2021**, *143*, 20166–20175.
- (53) Rupp, M. Machine learning for quantum mechanics in a nutshell. *Int. J. Quantum Chem.* **2015**, *115*, 1058–1073.
- (54) Knowles, P. J.; Werner, H.-J. An efficient second-order MC SCF method for long configuration expansions. *Chem. Phys. Lett.* **1985**, *115*, 259–267.

- (55) Werner, H.; Knowles, P. J. A second order multi-configuration SCF procedure with optimum convergence. *J. Chem. Phys.* **1985**, *82*, 5053–5063.
- (56) Frisch, M. J.; Trucks, G. W.; Schlegel, H. B.; Scuseria, G. E.; Robb, M. A.; Cheeseman, J. R.; Scalmani, G.; Barone, V.; Petersson, G. A.; Nakatsuji, H.; Li, X.; Caricato, M.; Marenich, A. V.; Bloino, J.; Janesko, B. G.; Gomperts, R.; Mennucci, B.; Hratchian, H. P.; Ortiz, J. V.; Izmaylov, A. F.; Sonnenberg, J. L.; Williams-Young, D.; Ding, F.; Lipparini, F.; Egidi, F.; Goings, J.; Peng, B.; Petrone, A.; Henderson, T.; Ranasinghe, D.; Zakrzewski, V. G.; Gao, J.; Rega, N.; Zheng, G.; Liang, W.; Hada, M.; Ehara, M.; Toyota, K.; Fukuda, R.; Hasegawa, J.; Ishida, M.; Nakajima, T.; Honda, Y.; Kitao, O.; Nakai, H.; Vreven, T.; Throssell, K.; Montgomery, J. A., Jr.; Peralta, J. E.; Ogliaro, F.; Bearpark, M. J.; Heyd, J. J.; Brothers, E. N.; Kudin, K. N.; Staroverov, V. N.; Keith, T. A.; Kobayashi, R.; Normand, J.; Raghavachari, K.; Rendell, A. P.; Burant, J. C.; Iyengar, S. S.; Tomasi, J.; Cossi, M.; Millam, J. M.; Klene, M.; Adamo, C.; Cammi, R.; Ochterski, J. W.; Martin, R. L.; Morokuma, K.; Farkas, O.; Foresman, J. B.; Fox, D. J. Gaussian®16 Revision C.01. 2016; Gaussian Inc. Wallingford CT.
- (57) Werner, H.-J.; Knowles, P. J.; Knizia, G.; Manby, F. R.; Schütz, M., et al. MOLPRO, version , a package of ab initio programs.
- (58) Manaa, M. R.; Yarkony, D. R. On the intersection of two potential energy surfaces of the same symmetry. Systematic characterization using a Lagrange multiplier constrained procedure. *J. Chem. Phys.* **1993**, *99*, 5251–5256.
- (59) Bishop, C. M.; Nasrabadi, N. M. *Pattern recognition and machine learning*; Springer, 2006; Vol. 4.
- (60) Pedregosa, F.; Varoquaux, G.; Gramfort, A.; Michel, V.; Thirion, B.; Grisel, O.; Blondel, M.; Prettenhofer, P.; Weiss, R.; Dubourg, V.; Vanderplas, J.; Passos, A.; Cournapeau, D.; Brucher, M.; Perrot, M.; Duchesnay, E. Scikit-learn: Machine Learning in Python. *J. Mach. Learn. Res.* **2011**, *12*, 2825–2830.
- (61) Dahl, J. P.; Springborg, M. The Morse oscillator in position space, momentum space, and phase space. *J. Chem. Phys.* **1988**, *88*, 4535–4547.
- (62) Schinke, R. *Photodissociation Dynamics: Spectroscopy and Fragmentation of Small Polyatomic Molecules*; Cambridge University Press, 1995.
- (63) Du, L.; Lan, Z. An On-the-Fly Surface-Hopping Program JADE for Nonadiabatic Molecular Dynamics of Polyatomic Systems: Implementation and Applications. *J. Chem. Theory Comput.* **2015**, *11*, 1360–1374.
- (64) Tannor, D. Introduction to Quantum Mechanics: A Time-Dependent Perspective. *University Science books: Mill Valley, U.S.A* **2007**,
- (65) Granucci, G.; Persico, M. Critical appraisal of the fewest switches algorithm for surface hopping. *J. Chem. Phys.* **2007**, *126*, 134114.
- (66) Hu, D.; Liu, Y. F.; Sobolewski, A. L.; Lan, Z. Nonadiabatic dynamics simulation of keto isocytosine: a comparison of dynamical performance of different electronic-structure methods. *Phys. Chem. Chem. Phys.* **2017**, *19*, 19168–19177.
- (67) Hu, D.; Peng, J.; Chen, L.; Gelin, M. F.; Lan, Z. Spectral Fingerprint of Excited-State Energy Transfer in Dendrimers through Polarization-Sensitive Transient-Absorption Pump-Probe Signals: On-the-Fly Nonadiabatic Dynamics Simulations. *J. Phys. Chem. Lett.* **2021**, *12*, 9710–9719.
- (68) Diau, E. W.-G.; Zewail, A. H. Femtochemistry of trans-Azomethane: A Combined Experimental and Theoretical Study. *ChemPhysChem* **2003**, *4*, 445–456.
- (69) Mandal, A.; Vega, S. M.; Huo, P. Polarized Fock States and the Dynamical Casimir Effect in Molecular Cavity Quantum Electrodynamics. *J. Phys. Chem. Lett.* **2020**, *11*, 9215–9223.
- (70) Schäfer, C.; Ruggenthaler, M.; Rokaj, V.; Rubio, A. Relevance of the Quadratic Diamagnetic and Self-Polarization Terms in Cavity Quantum Electrodynamics. *ACS Photonics* **2020**, *7*, 975–990.
- (71) Power, E. A.; Zienau, S. Coulomb Gauge in Non-relativistic Quantum Electro-Dynamics and the Shape of Spectral Lines. *Philos. Trans. R. Soc. London, Ser. A* **1959**, *251*, 427–454.
- (72) Cohen-Tannoudji, C.; Dupont-Roc, J.; Grynberg, G. Photons and Atoms: Introduction to Quantum Electrodynamics. *John Wiley & Sons, Inc.* **1989**,
- (73) Taylor, M. A. D.; Mandal, A.; Zhou, W.; Huo, P. Resolution of Gauge Ambiguities in Molecular Cavity Quantum Electrodynamics. *Phys. Rev. Lett.* **2020**, *125*, 123602.
- (74) Schirmer, J. Beyond the random-phase approximation: A new approximation scheme for the polarization propagator. *Phys. Rev. A* **1982**, *26*, 2395–2416.

- (75) Trofimov, A. B.; Schirmer, J. An efficient polarization propagator approach to valence electron excitation spectra. *J. Phys. B* **1995**, *28*, 2299.
- (76) Runge, E.; Gross, E. K. U. Density-Functional Theory for Time-Dependent Systems. *Phys. Rev. Lett.* **1984**, *52*, 997–1000.
- (77) Gross, E. K. U.; Kohn, W. Local density-functional theory of frequency-dependent linear response. *Phys. Rev. Lett.* **1985**, *55*, 2850–2852.

**Supporting Information for
Ab-initio Molecular Cavity Quantum Electrodynamics
Simulations Using Machine Learning Models**

Deping Hu^{*}

*Department of Chemistry, University of Rochester,
120 Trustee Road, Rochester, NY 14627, U.S.A.*

Pengfei Huo[†]

*Department of Chemistry, University of Rochester,
120 Trustee Road, Rochester, NY 14627, U.S.A. and
The Institute of Optics, Hajim School of Engineering,
University of Rochester, Rochester, New York, 14627, U.S.A.*

I. RELATIVE CARTESIAN COORDINATE SYSTEM

The definition of the relative Cartesian coordinate system is shown in Figure S1. We choose three different atoms (A, B and C) of the molecule as the reference atoms. For the azomethane molecule studied in this work, A and B are the two Nitrogen atoms, and C is one of the Carbon atoms. Then X-axis of the relative Cartesian coordinate system is defined along the $A \rightarrow B$ direction, the Y-axis is defined perpendicular to the plane formed by ABC, and the Z-axis is defined perpendicular to the X- and Y-axes simultaneously. We emphasize that we need to define individual relative coordinate systems for each of the conformers in the training dataset, since the positions of A, B and C atoms could vary for different conformers. Nevertheless, by using these three atoms, we uniquely define the 3 axes.

After we define the relative Cartesian coordinate system, we further transform the dipole based on the original Cartesian coordinate system in space (referred to as the global Cartesian coordinate system in this work) to the newly-defined relative Cartesian coordinate system. Below, we present details of the coordinate system transformation.

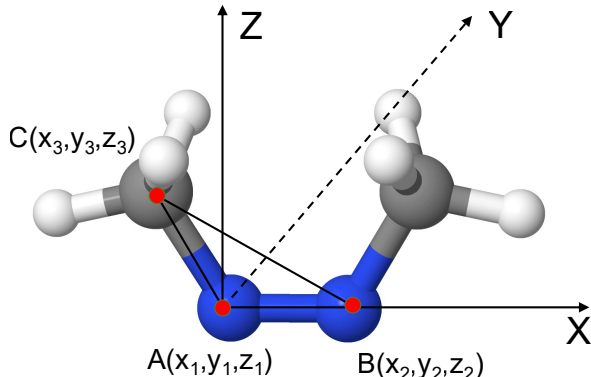


FIG. S1: Relative Cartesian coordinate system defined in this work. A, B and C are three reference atoms of the molecular system. For the azomethane molecule, A and B are the two Nitrogen atoms, and C is one of the Carbon atoms. For the relative Cartesian coordinate system, the X-axis is defined along the $A \rightarrow B$ direction, the Y-axis is defined perpendicular to the plane formed by ABC, and the Z-axis is defined perpendicular to the X- and Y-axes simultaneously.

The first step is to obtain the unit vectors along the X-, Y- and Z-axis directions (\vec{x} , \vec{y}

and \vec{z}), expressed as follows

$$\vec{x} = (a_1, b_1, c_1) \quad (\text{S1a})$$

$$\vec{y} = (a_2, b_2, c_3) \quad (\text{S1b})$$

$$\vec{z} = (a_3, b_3, c_3). \quad (\text{S1c})$$

Here, we already know the positions of A, B and C based on the global Cartesian coordinate system, which are (x_1, y_1, z_1) , (x_2, y_2, z_2) and (x_3, y_3, z_3) , respectively. Since the X-axis is along the $A \rightarrow B$ direction, we can express \vec{x} with its coordinate as

$$a_1 = \frac{(x_2 - x_1)}{\sqrt{((x_2 - x_1)^2 + (y_2 - y_1)^2 + (z_2 - z_1)^2)}} \quad (\text{S2a})$$

$$b_1 = \frac{(y_2 - y_1)}{\sqrt{((x_2 - x_1)^2 + (y_2 - y_1)^2 + (z_2 - z_1)^2)}} \quad (\text{S2b})$$

$$c_1 = \frac{(z_2 - z_1)}{\sqrt{((x_2 - x_1)^2 + (y_2 - y_1)^2 + (z_2 - z_1)^2)}}. \quad (\text{S2c})$$

Next, considering the Y-axis is perpendicular to the plane formed by ABC, we can write the equation for the plane formed by ABC as $mx + ny + kz + l = 0$, where

$$\begin{aligned} m &= y_1(z_2 - z_3) + y_2(z_3 - z_1) + y_3(z_1 - z_2) \\ n &= z_1(x_2 - x_3) + z_2(x_3 - x_1) + z_3(x_1 - x_2) \\ k &= x_1(y_2 - y_3) + x_2(y_3 - y_1) + x_3(y_1 - y_2) \\ l &= -x_1(y_2z_3 - y_3z_2) - x_2(y_3z_1 - y_1z_3) - x_3(y_1z_2 - y_2z_1). \end{aligned} \quad (\text{S3a})$$

We can further express \vec{y} using the coordinates as

$$a_2 = \frac{m}{\sqrt{m^2 + n^2 + k^2}} \quad (\text{S4a})$$

$$b_2 = \frac{n}{\sqrt{m^2 + n^2 + k^2}} \quad (\text{S4b})$$

$$c_2 = \frac{k}{\sqrt{m^2 + n^2 + k^2}}. \quad (\text{S4c})$$

Finally, the Z-axis is perpendicular to the X- and Y-axes simultaneously, which means that $\vec{z} = \vec{x} \times \vec{y}$, resulting in

$$a_3 = b_1c_2 - b_2c_1 \quad (\text{S5a})$$

$$b_3 = a_2c_1 - a_1c_2 \quad (\text{S5b})$$

$$c_3 = a_1b_2 - a_2b_1. \quad (\text{S5c})$$

Until now, we get the unit vectors of the axes of the relative Cartesian system. Next, we need to project the dipole to the new axes. Given the dipole based on the global Cartesian coordinate system as

$$\vec{\mu}^g = (\mu_x^g, \mu_y^g, \mu_z^g), \quad (\text{S6})$$

where the notation g denotes the dipole based on the global Cartesian coordinate system. Assuming the dipole based on the relative Cartesian coordinate system is

$$\vec{\mu}^r = (\mu_x^r, \mu_y^r, \mu_z^r), \quad (\text{S7})$$

which can be obtained through the following projection equation

$$\mu_x^r = \vec{\mu}^g \cdot \vec{x} = \mu_x^g a_1 + \mu_y^g b_1 + \mu_z^g c_1 \quad (\text{S8a})$$

$$\mu_y^r = \vec{\mu}^g \cdot \vec{y} = \mu_x^g a_2 + \mu_y^g b_2 + \mu_z^g c_2 \quad (\text{S8b})$$

$$\mu_z^r = \vec{\mu}^g \cdot \vec{z} = \mu_x^g a_3 + \mu_y^g b_3 + \mu_z^g c_3. \quad (\text{S8c})$$

We can further write Eq. S8 in a matrix representation as

$$\begin{pmatrix} \mu_x^r \\ \mu_y^r \\ \mu_z^r \end{pmatrix} = \begin{pmatrix} a_1 & b_1 & c_1 \\ a_2 & b_2 & c_2 \\ a_3 & b_3 & c_3 \end{pmatrix} \begin{pmatrix} \mu_x^g \\ \mu_y^g \\ \mu_z^g \end{pmatrix}. \quad (\text{S9})$$

In this work, we use $\vec{\mu}^r$ instead of $\vec{\mu}^g$ in the training process. In the prediction process, since the predicated value is also $\vec{\mu}^r$, we need to transform it back to $\vec{\mu}^g$ using the following equation

$$\begin{pmatrix} \mu_x^g \\ \mu_y^g \\ \mu_z^g \end{pmatrix} = \begin{pmatrix} d_1 & e_1 & f_1 \\ d_2 & e_2 & f_2 \\ d_3 & e_3 & f_3 \end{pmatrix} \begin{pmatrix} \mu_x^r \\ \mu_y^r \\ \mu_z^r \end{pmatrix}, \quad (\text{S10})$$

where

$$\begin{pmatrix} d_1 & e_1 & f_1 \\ d_2 & e_2 & f_2 \\ d_3 & e_3 & f_3 \end{pmatrix} = \begin{pmatrix} a_1 & b_1 & c_1 \\ a_2 & b_2 & c_2 \\ a_3 & b_3 & c_3 \end{pmatrix}^{-1} = \frac{1}{q} \begin{pmatrix} b_2 c_3 - c_2 b_3 & c_1 b_3 - b_1 c_3 & b_1 c_2 - c_1 b_2 \\ c_2 a_3 - a_2 c_3 & a_1 c_3 - c_1 a_3 & a_2 c_1 - a_1 c_2 \\ a_2 b_3 - b_2 a_3 & b_1 a_3 - a_1 b_3 & a_1 b_2 - a_2 b_1 \end{pmatrix}, \quad (\text{S11})$$

and

$$q = a_1 (b_2 c_3 - c_2 b_3) - a_2 (b_1 c_3 - c_1 b_3) + a_3 (b_1 c_2 - c_1 b_2). \quad (\text{S12})$$

Using Eq. S10, we obtain

$$\begin{aligned}\mu_x^g &= \mu_x^r d_1 + \mu_y^r e_1 + \mu_z^r f_1 \\ \mu_y^g &= \mu_x^r d_2 + \mu_y^r e_2 + \mu_z^r f_2 \\ \mu_z^g &= \mu_x^r d_3 + \mu_y^r e_3 + \mu_z^r f_3.\end{aligned}\quad (\text{S13a})$$

The derivative of the dipole on one of the nuclear DOF R_i^g based on the global Cartesian coordinate is expressed as follows

$$\frac{\partial \mu_x^g}{\partial R_i^g} = \frac{\partial \mu_x^r}{\partial R_i^g} d_1 + \mu_x^r \frac{\partial d_1}{\partial R_i^g} + \frac{\partial \mu_y^r}{\partial R_i^g} e_1 + \mu_y^r \frac{\partial e_1}{\partial R_i^g} + \frac{\partial \mu_z^r}{\partial R_i^g} f_1 + \mu_z^r \frac{\partial f_1}{\partial R_i^g} \quad (\text{S14a})$$

$$\frac{\partial \mu_y^g}{\partial R_i^g} = \frac{\partial \mu_x^r}{\partial R_i^g} d_2 + \mu_x^r \frac{\partial d_2}{\partial R_i^g} + \frac{\partial \mu_y^r}{\partial R_i^g} e_2 + \mu_y^r \frac{\partial e_2}{\partial R_i^g} + \frac{\partial \mu_z^r}{\partial R_i^g} f_2 + \mu_z^r \frac{\partial f_2}{\partial R_i^g} \quad (\text{S14b})$$

$$\frac{\partial \mu_z^g}{\partial R_i^g} = \frac{\partial \mu_x^r}{\partial R_i^g} d_3 + \mu_x^r \frac{\partial d_3}{\partial R_i^g} + \frac{\partial \mu_y^r}{\partial R_i^g} e_3 + \mu_y^r \frac{\partial e_3}{\partial R_i^g} + \frac{\partial \mu_z^r}{\partial R_i^g} f_3 + \mu_z^r \frac{\partial f_3}{\partial R_i^g}. \quad (\text{S14c})$$

We can also re-express the above expression (Eq. S14) in a matrix representation as

$$\begin{pmatrix} \frac{\partial \mu_x^g}{\partial R_i^g} \\ \frac{\partial \mu_y^g}{\partial R_i^g} \\ \frac{\partial \mu_z^g}{\partial R_i^g} \end{pmatrix} = \begin{pmatrix} d_1 & e_1 & f_1 \\ d_2 & e_2 & f_2 \\ d_3 & e_3 & f_3 \end{pmatrix} \begin{pmatrix} \frac{\partial \mu_x^r}{\partial R_i^g} \\ \frac{\partial \mu_y^r}{\partial R_i^g} \\ \frac{\partial \mu_z^r}{\partial R_i^g} \end{pmatrix} + \begin{pmatrix} \frac{\partial d_1}{\partial R_i^g} & \frac{\partial e_1}{\partial R_i^g} & \frac{\partial f_1}{\partial R_i^g} \\ \frac{\partial d_2}{\partial R_i^g} & \frac{\partial e_2}{\partial R_i^g} & \frac{\partial f_2}{\partial R_i^g} \\ \frac{\partial d_3}{\partial R_i^g} & \frac{\partial e_3}{\partial R_i^g} & \frac{\partial f_3}{\partial R_i^g} \end{pmatrix} \begin{pmatrix} \mu_x^r \\ \mu_y^r \\ \mu_z^r \end{pmatrix}. \quad (\text{S15})$$

On the right-hand side of the above expression, the transformation matrix between the global Cartesian coordinate and the relative Cartesian coordinate can be obtained through Eq. S11. The derivative of the transformation matrix can be obtained by expanding Eq. S11 in terms of the global Cartesian coordinate. The dipoles and their derivatives can be obtained through the machine learning model.

In principle, the analytical expression of the derivative of the transformation matrix in terms of the global Cartesian coordinate, such as $\frac{\partial d_1}{\partial R_i^g}$, can be derived with the SymPy¹ library of Python. However, the expression is extremely tedious and it is actually time-consuming to apply the analytical expression to get the derivative in the dynamics process. A practical way is to get the derivatives numerically, with the following expression (take $\frac{\partial d_1}{\partial R_i^g}$ for example)

$$\frac{\partial d_1(R_i^g)}{\partial R_i^g} = \frac{d_1(R_i^g + \delta R_i^g) - d_1(R_i^g - \delta R_i^g)}{2\delta R_i^g}. \quad (\text{S16})$$

In our model, R_i^g is set to be 0.001 a.u. to get the converged results. This is what we used in the actual numerical implementation.

II. DISTRIBUTION OF THE CNNC DIHEDRAL ANGLES IN THE TRAINING DATASET

The distribution of the CNNC dihedral angles for azomethane in the final training dataset is shown in Fig. S2. We can see that the dihedral angles are well distributed (although not uniformly) from -180 to 180 degrees. Thus, the training dataset is properly sampled in this work.

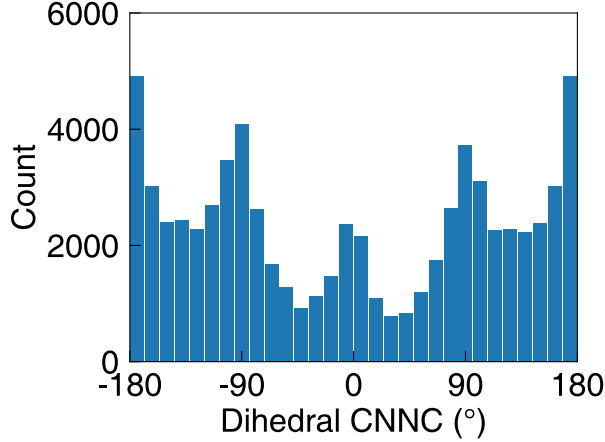


FIG. S2: Distributions of the CNNC dihedral angles in the training dataset.

III. KERNEL RIDGE REGRESSION ERROR

To check the accuracy of the machine learning dipoles constructed in this work, we plot the distribution of the test errors in the learning procedure, as shown in Fig. S3. For the azomethane molecule studied in this work, there are two kinds of permanent dipoles (ground and excited states permanent dipoles) and one transition dipole (ground to excited state transition dipole), and each dipole has three components in different directions (X, Y, Z). Thus, we have nine different dipole components and we trained and tested them separately. Fig. S3 shows that the Kernel ridge regression method can well predict the permanent and transition dipoles for all components in different directions, with small mean average errors.

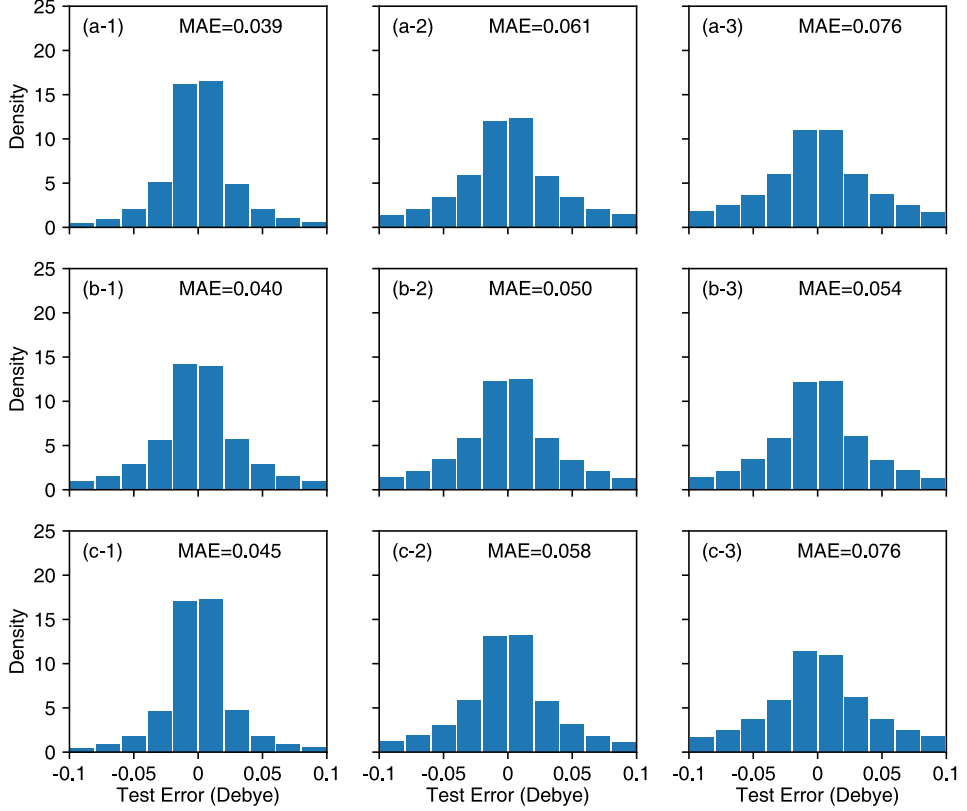


FIG. S3: Distributions of the test errors in the machine learning model for (a) permanent dipole of ground state, (b) transition dipole between ground state and excited state, and (c) permanent dipole of excited state, in different directions: (1) X-axis (left column), (2) Y-axis (middle column) and (3) Z-axis (right column).

IV. POLARITON POTENTIAL ENERGY SURFACE WITH DIFFERENT HAMILTONIANS

In the investigations of polariton photochemistry, besides the Pauli-Fierz (PF) Hamiltonian used in this work, several other Hamiltonian models have been used to describe the quantum light-matter interactions in previous studies, for example, the Jaynes-Cummings (JC) model^{2,3} and Rabi model.⁴ Next we will derive these models from the PF model Hamiltonian. We write the PF Hamiltonian below for convenience,

$$\begin{aligned} \hat{H}^{\text{PF}} &= \hat{T}_n + \hat{H}_{\text{en}} + \hat{H}_p + \hat{H}_{\text{enp}} + \hat{H}_d \\ &= \hat{T}_n + \hat{H}_{\text{en}} + \hat{H}_p + g_c \boldsymbol{\epsilon} \cdot \hat{\boldsymbol{\mu}} (\hat{a}^\dagger + \hat{a}) + \frac{g_c^2}{\hbar \omega_c} (\boldsymbol{\epsilon} \cdot \hat{\boldsymbol{\mu}})^2. \end{aligned} \quad (\text{S17})$$

Take the azomethane molecule studied in this work as an example, only two electronic states $\{|g\rangle, |e\rangle\}$ are considered during the dynamics, the transition dipole between them is defined as $\boldsymbol{\mu}_{ge} = \langle g|\hat{\boldsymbol{\mu}}|e\rangle$. If we ignore the permanent dipole moments (PDMs) and further define the creation and annihilation operators for molecular excitation as $\hat{\sigma}^\dagger \equiv |e\rangle\langle g|$ and $\hat{\sigma} \equiv |g\rangle\langle e|$, the dipole operator can be written as $\hat{\boldsymbol{\mu}} = \boldsymbol{\mu}_{eg} \cdot (\hat{\sigma}^\dagger + \hat{\sigma})$. The molecule-cavity interaction term can now be expressed as

$$\hat{H}_{enp} = g_c \boldsymbol{\epsilon} \cdot \boldsymbol{\mu}_{eg} \cdot (\hat{a}^\dagger + \hat{a})(\hat{\sigma}^\dagger + \hat{\sigma}). \quad (\text{S18})$$

If we further drop the dipole self-energy (DSE) term \hat{H}_d , we can obtain the Rabi model as

$$\hat{H}^{\text{Rabi}} = \hat{T}_n + \hat{H}_{en} + \hat{H}_p + g_c \boldsymbol{\epsilon} \cdot \boldsymbol{\mu}_{eg} \cdot (\hat{a}^\dagger + \hat{a})(\hat{\sigma}^\dagger + \hat{\sigma}). \quad (\text{S19})$$

Assuming the rotation wave approximation by ignoring the counter-rotating terms $\hat{a}^\dagger \hat{\sigma}^\dagger$ and $\hat{a} \hat{\sigma}$, we can arrive at the JC model,

$$\hat{H}^{\text{JC}} = \hat{T}_n + \hat{H}_{en} + \hat{H}_p + g_c \boldsymbol{\epsilon} \cdot \boldsymbol{\mu}_{eg} \cdot (\hat{a}^\dagger \hat{\sigma} + \hat{a} \hat{\sigma}^\dagger). \quad (\text{S20})$$

Here we introduce two other models for comparison, namely the PF Hamiltonian without the DSE term,

$$\hat{H}^{\text{NDSE}} = \hat{T}_n + \hat{H}_{en} + \hat{H}_p + g_c \boldsymbol{\epsilon} \cdot \hat{\boldsymbol{\mu}} (\hat{a}^\dagger + \hat{a}), \quad (\text{S21})$$

and the PF Hamiltonian without the PDM,

$$\hat{H}^{\text{NPDM}} = \hat{T}_n + \hat{H}_{en} + \hat{H}_p + g_c \boldsymbol{\epsilon} \cdot \boldsymbol{\mu}_{eg} \cdot (\hat{a}^\dagger + \hat{a})(\hat{\sigma}^\dagger + \hat{\sigma}) + \frac{g_c^2}{\hbar \omega_c} (\boldsymbol{\epsilon} \cdot \boldsymbol{\mu}_{eg})^2. \quad (\text{S22})$$

Until now, we have four additional Hamiltonian models, which are the Rabi model, JC model, PF model without PDM, and PF model without DSE. To investigate the roles of the DSE term and PDM play in the formation of the polaritonic states, we plot the potential energy surfaces (PESs) of the polaritonic states for azomethane molecule based on these models and compare them with that based on the PF model. The results with the field polarized along the Y-axis and Z-axis are presented in Fig. S4 and Fig. S5, respectively.

When the field is polarized along the Y-axis, the transition dipole is much larger than the permanent dipole, and the polariton PESs with different Hamiltonian models are shown in Fig. S4. For low-lying polaritonic states ($|\mathcal{E}_0\rangle, |\mathcal{E}_1\rangle, |\mathcal{E}_2\rangle, |\mathcal{E}_3\rangle$), the polariton PESs with all Hamiltonian models are in a good agreement. For high-lying polaritonic states ($|\mathcal{E}_4\rangle, |\mathcal{E}_5\rangle$), only the Rabi and JC models show obvious discrepancy compared to the PF Hamiltonian.

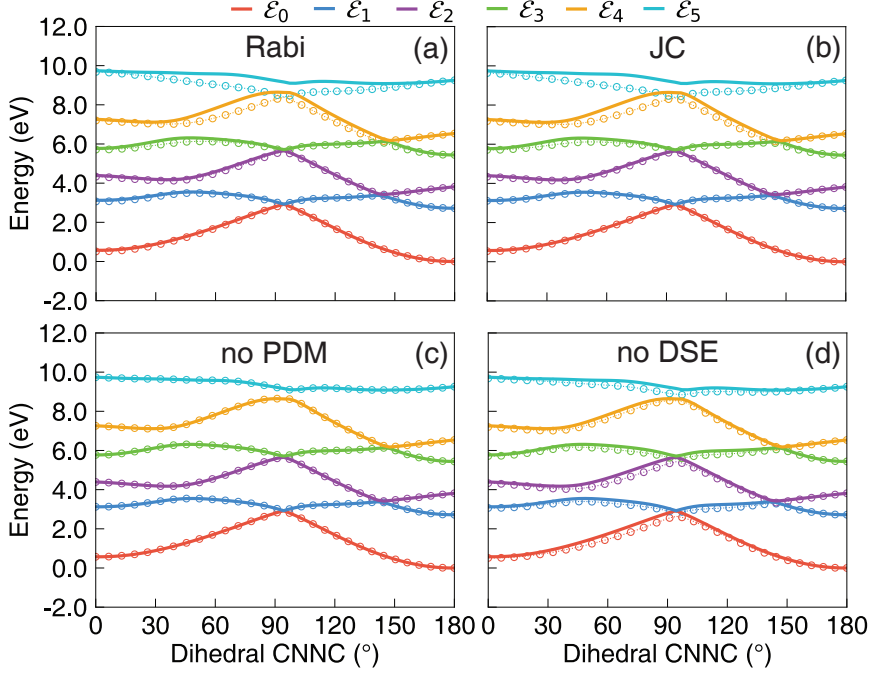


FIG. S4: Comparison of the PESs of the polaritonic states for azomethane molecule inside the cavity generated from the PF Hamiltonian (solid lines) with other four different Hamiltonian models (open circles): (a) Rabi model; (b) JC model; (c) PF model without the PDM; (d) PF model without the DSE. The light-matter coupling strength is $g_c = 0.05$ a.u. and the field is polarized along the Y-axis. The cavity frequency is set to $\hbar\omega_c = 2.72$ eV.

Considering only some low-lying polaritonic states are populated during the dynamics for the molecular system studied in this work, we expect that polariton dynamics based on all the Hamiltonian models are similar in the case when the field is polarized along the Y-axis.

When the field is polarized along the Z-axis, the permanent dipole is much larger than the transition dipole, and the PESs with different Hamiltonian models are shown in Fig. S5. In this case, compared to the PESs obtained from the PF model, the PESs obtained from the other four Hamiltonian models (Rabi, JC, PF no PDM, PF no DSE) are much different. This large discrepancy is caused by large permanent dipoles for both $|g\rangle$ and $|e\rangle$ (see Fig. 2d of the main text). The light-matter interaction terms related to the permanent dipoles are completely ignored by the quantum optics model Hamiltonians, causing a large difference in polariton potentials compared to the full PH Hamiltonian treatment. As a result, the polariton dynamics should also be less accurate if we take these approximated Hamiltonian models instead of using the full PF model in the case when the field is polarized along the

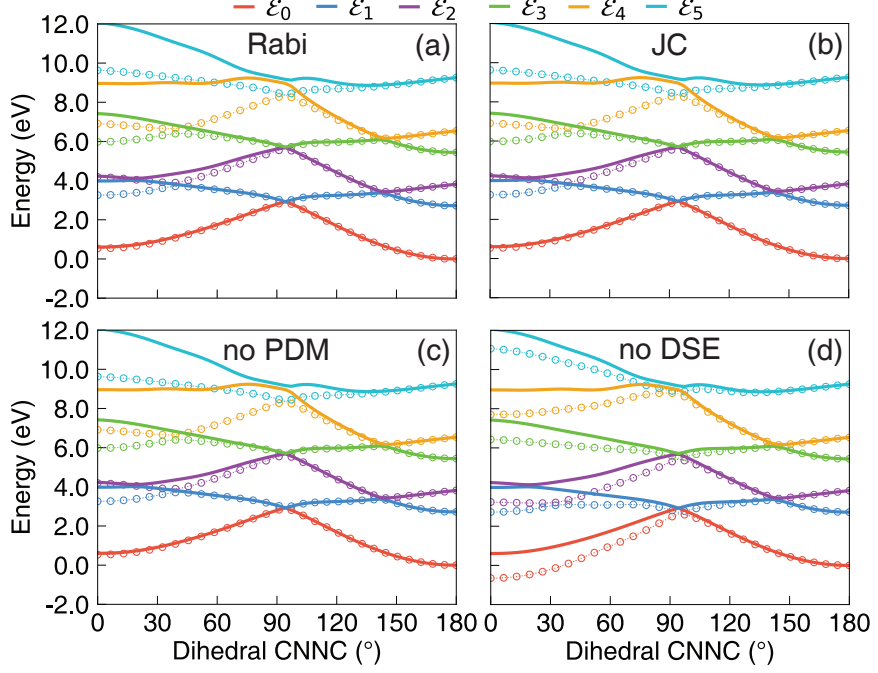


FIG. S5: Comparison of the polariton potential energy surface of the azomethane molecule coupled inside the cavity, obtained from the PF Hamiltonian (solid lines) with other four different Hamiltonian models (open circles), including (a) Rabi model; (b) JC model; (c) PF model without the PDM; (d) PF model without the DSE. The light-matter coupling strength is $g_c = 0.05$ a.u. and the field is polarized along the Z-axis. The cavity frequency is set to $\hbar\omega_c = 2.72$ eV.

Z-axis.

V. PHOTON NUMBER OPERATOR IN THE DIPOLE GAUGE

We provide a brief derivation of the “photon number” operator under the *dipole* gauge (the “ $d \cdot E$ ” form) used in the Pauli-Fierz (PF) Hamiltonian, where the details can be found in the related previous work.^{5,6} Under the *Coulomb* gauge (the “ $p \cdot A$ ” form of light-matter interactions), the photon number operator is expressed as

$$\hat{N}_{p \cdot A} = \hat{a}^\dagger \hat{a} = \frac{1}{2\hbar\omega_c} \hat{p}_c^2 + \frac{\omega_c}{2\hbar} \hat{q}_c^2 - \frac{1}{2}. \quad (\text{S23})$$

Under the *dipole* gauge, the “photon number” operator should be

$$\begin{aligned}\hat{N}_{\text{d.E}} &= \hat{U}\hat{a}^\dagger\hat{a}\hat{U}^\dagger = \hat{U}\hat{a}^\dagger\hat{U}^\dagger\hat{U}\hat{a}\hat{U}^\dagger \\ &= \frac{1}{2\hbar\omega_c}(\hat{p}_c + g_c\sqrt{\frac{2}{\hbar\omega_c^3}}\hat{\mu}\cdot\epsilon)^2 + \frac{\omega_c}{2\hbar}\hat{q}_c^2 - \frac{1}{2},\end{aligned}\quad (\text{S24})$$

where

$$\hat{U} = \exp\left[-\frac{i}{\hbar}\hat{\mu}\cdot\epsilon\frac{g_c}{\omega_c^2}(\hat{a} + \hat{a}^\dagger)\right], \quad (\text{S25})$$

is the Power-Zienau-Woolley (PZW) Gauge transformation operator.^{7,8} The “photon number” operator for the PF Hamiltonian can be obtained by using the following unitary transformation

$$\hat{N}_{\text{PF}} = \hat{U}_\phi\hat{N}_{\text{d.E}}\hat{U}_\phi^\dagger = \frac{1}{2\hbar\omega_c}\hat{p}_c^2 + \frac{\omega_c}{2\hbar}(\hat{q}_c + g_c\sqrt{\frac{2}{\hbar\omega_c^3}}\hat{\mu}\cdot\epsilon)^2 - \frac{1}{2}, \quad (\text{S26})$$

where

$$\hat{U}_\phi = \exp[-i\frac{\pi}{2}\hat{a}^\dagger\hat{a}]. \quad (\text{S27})$$

One can further express Eq. S26 as

$$\begin{aligned}\hat{N}_{\text{PF}} &= \frac{1}{2\hbar\omega_c}\hat{p}_c^2 + \frac{\omega_c}{2\hbar}(\hat{q}_c + g_c\sqrt{\frac{2}{\hbar\omega_c^3}}\hat{\mu}\cdot\epsilon)^2 - \frac{1}{2} \\ &= \frac{1}{2\hbar\omega_c}\hat{p}_c^2 + \frac{\omega_c}{2\hbar}\hat{q}_c^2 + \frac{\omega_c}{2\hbar}\hat{q}_c g_c\sqrt{\frac{2}{\hbar\omega_c^3}}\hat{\mu}\cdot\epsilon + \frac{\omega_c}{2\hbar}g_c\sqrt{\frac{2}{\hbar\omega_c^3}}\hat{\mu}\cdot\epsilon\hat{q}_c + \frac{\omega_c}{2\hbar}(g_c\sqrt{\frac{2}{\hbar\omega_c^3}}\hat{\mu}\cdot\epsilon)^2 - \frac{1}{2} \\ &= \hat{a}^\dagger\hat{a} + \frac{\omega_c}{2\hbar}\hat{q}_c g_c\sqrt{\frac{2}{\hbar\omega_c^3}}\hat{\mu}\cdot\epsilon + \frac{\omega_c}{2\hbar}g_c\sqrt{\frac{2}{\hbar\omega_c^3}}\hat{\mu}\cdot\epsilon\hat{q}_c + \frac{\omega_c}{2\hbar}(g_c\sqrt{\frac{2}{\hbar\omega_c^3}}\hat{\mu}\cdot\epsilon)^2 \\ &= \hat{a}^\dagger\hat{a} + \frac{\omega_c}{2\hbar}\sqrt{\frac{\hbar}{2\omega_c}}(\hat{a}^\dagger + \hat{a})g_c\sqrt{\frac{2}{\hbar\omega_c^3}}\hat{\mu}\cdot\epsilon + \frac{\omega_c}{2\hbar}g_c\sqrt{\frac{2}{\hbar\omega_c^3}}\hat{\mu}\cdot\epsilon\sqrt{\frac{\hbar}{2\omega_c}}(\hat{a}^\dagger + \hat{a}) + \frac{\omega_c}{2\hbar}(g_c\sqrt{\frac{2}{\hbar\omega_c^3}}\hat{\mu}\cdot\epsilon)^2 \\ &= \hat{a}^\dagger\hat{a} + \frac{g_c}{2\omega_c\hbar}(\hat{a}^\dagger + \hat{a})\hat{\mu}\cdot\epsilon + \frac{g_c}{2\omega_c\hbar}\hat{\mu}\cdot\epsilon(\hat{a}^\dagger + \hat{a}) + \frac{\omega_c}{2\hbar}(g_c\sqrt{\frac{2}{\hbar\omega_c^3}}\hat{\mu}\cdot\epsilon)^2 \\ &= \hat{a}^\dagger\hat{a} + \frac{g_c}{\omega_c\hbar}\hat{\mu}\cdot\epsilon(\hat{a}^\dagger + \hat{a}) + \frac{g_c^2}{\omega_c^2\hbar^2}(\hat{\mu}\cdot\epsilon)^2 \\ &= \hat{a}^\dagger\hat{a} + \frac{1}{\hbar\omega_c}(\hat{H}_{\text{enp}} + \hat{H}_{\text{d}}) \\ &= \frac{1}{\hbar\omega_c}(\hat{H}_{\text{p}} + \hat{H}_{\text{enp}} + \hat{H}_{\text{d}}) - \frac{1}{2}.\end{aligned}$$

VI. QED SIMULATIONS WITH FIELD POLARIZED ALONG THE Z-AXIS

As pointed out in Sec. 4.2 in the main text, the magnitudes of the dipoles (permanent and transition dipoles) for the azomethane molecule in different directions vary a lot. To

explore how the spatial orientation of the molecule affects the polariton dynamics, we also perform the QED simulation with field polarized along the Z-axis, which means $(\epsilon_x, \epsilon_y, \epsilon_z)$ is set to $(0, 0, 1)$ in Eq. 16 of the main text. Here, only the components of dipoles along the Z-axis contribute to the light-matter coupling. Same as the Y-polarized case, we consider two different light-matter coupling strengths: $g_c = 0.005$ a.u. and $g_c = 0.05$ a.u.

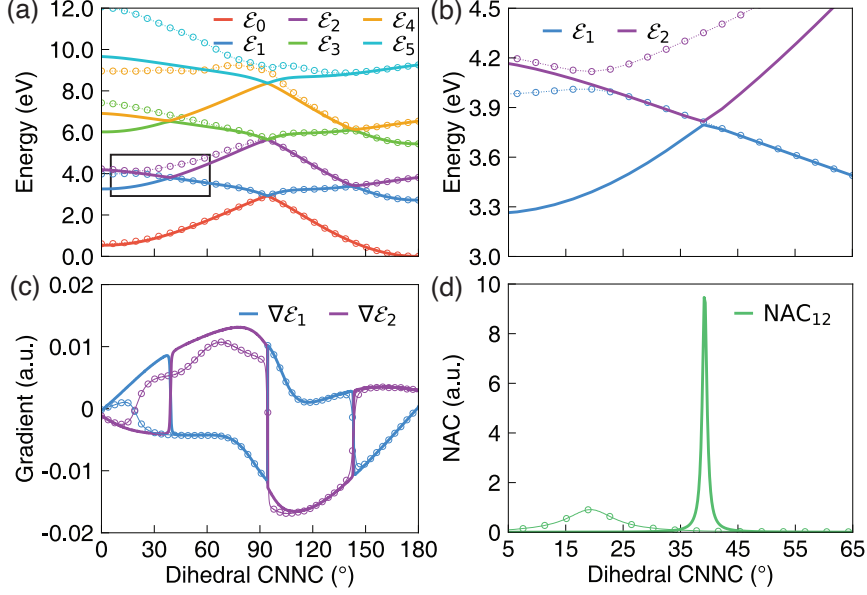


FIG. S6: The (a-b) PESs, (c) gradients and (d) NACs of the polaritonic states for azomethane molecule inside the cavity. The field is polarized along the Z-axis. The results obtained with the light-matter coupling strength $g_c = 0.005$ a.u. and $g_c = 0.05$ a.u. are plotted with solid lines and open circles, respectively. The cavity frequency is set to $\hbar\omega_c = 2.72$ eV.

When using $g_c = 0.005$ a.u., because the transition dipole along the Z-axis is small (Fig. 2d in the main text), the avoided crossing region between the $|\mathcal{E}_2\rangle$ and $|\mathcal{E}_1\rangle$ states becomes narrow with a very small Rabi splitting, as shown in Fig. S6a and Fig. S6b. Thus, the NAC between the $|\mathcal{E}_2\rangle$ and $|\mathcal{E}_1\rangle$ states (Fig. S6d) is much larger than that in the Y-polarized case (Fig. 3d in the main text). As a result, the polariton population transfers very fast from the $|\mathcal{E}_2\rangle$ state to the $|\mathcal{E}_1\rangle$ state at the beginning of the dynamics, see Fig. S7a. In addition, due to the small transition dipole, there is only a small amount of population transferred to the $|g1\rangle$ state from $|e0\rangle$ state (Fig. S7b). The features of the polariton dynamics, such as the population of the *trans* isomer (Fig. S7d) and the evolution of the dihedral CNNC angles (Fig. S8a) are also similar to those outside the cavity (Fig. 1c and 1d in the main text), due

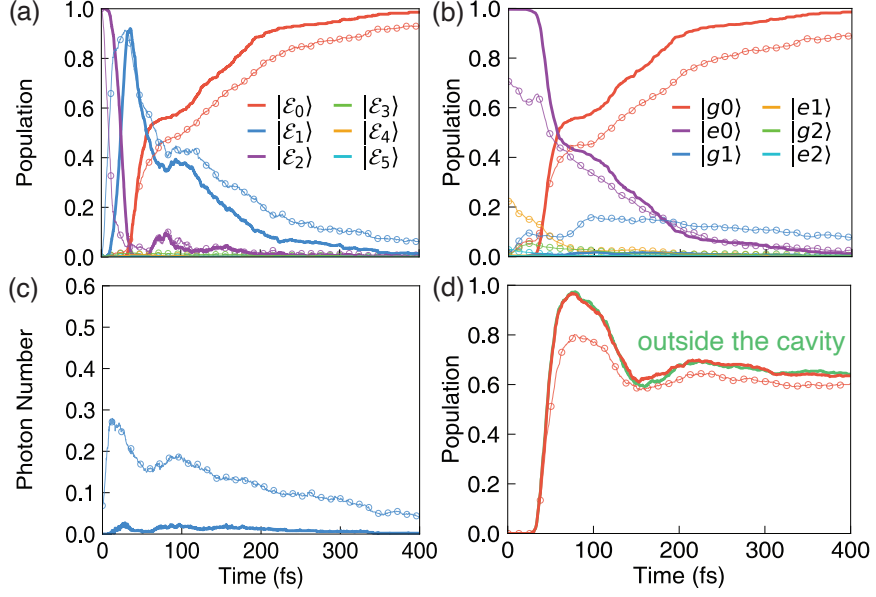


FIG. S7: The time-dependent properties in the QED simulation: (a) population of the polaritonic states; (b) population of the adiabatic-Fock states; (c) the average photon number population; (d) population of the *trans* isomer. The results obtained with the light-matter coupling strength $g_c = 0.005$ a.u. and $g_c = 0.05$ a.u. are plotted with solid lines and open circles, respectively. The cavity loss rate is set to $\Gamma = 4$ meV. The field is polarized along the Z-axis. The cavity frequency is set to $\hbar\omega_c = 2.72$ eV.

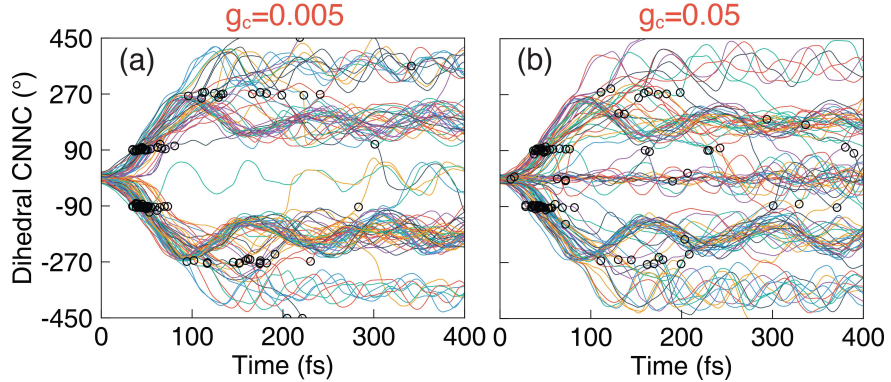


FIG. S8: The time-dependent values of the dihedral CNNC angles (of 100 trajectories) in the QED simulation for the azomethane molecule with light-matter coupling strength (a) $g_c = 0.005$ a.u. and (b) $g_c = 0.05$ a.u. The cavity loss rate is set to $\Gamma = 4$ meV. The field is polarized along the Z-axis. The cavity frequency is set to $\hbar\omega_c = 2.72$ eV. The black circles indicate where the hop events happen from the $|\mathcal{E}_1\rangle$ state to the $|\mathcal{E}_0\rangle$ state in the TSH dynamics.

to the small dipole and light-matter coupling strength.

When increasing the coupling strength to $g_c = 0.05$ a.u., comparing to the Y-polarized case with the same light-matter coupling strength, the most obvious difference is that the avoided crossing between the $|\mathcal{E}_2\rangle$ and $|\mathcal{E}_1\rangle$ states shifts to the *cis* isomer site with a smaller dihedral CNNC angle, see Fig. S6a and b. This is because the permanent dipoles dominate the light-matter coupling in this case, and the permanent dipole of the $|g\rangle$ state is larger than that of the $|e\rangle$ state, as shown in Fig. 2d in the main text. The crossing between the gradients of the $|\mathcal{E}_2\rangle$ and $|\mathcal{E}_1\rangle$ states and the peak of the NAC between them also shift, see Fig. S6c and Fig. S6d. Since the energy gap between the $|\mathcal{E}_2\rangle$ and $|\mathcal{E}_1\rangle$ states is close to each other near the Franck-Condon region, the system transforms very fast (within 30 fs) from the $|\mathcal{E}_2\rangle$ state to the $|\mathcal{E}_1\rangle$ state, see the open circles in Fig. S7a. After that, the system stays at the $|\mathcal{E}_1\rangle$ state for a longer time than the $g_c = 0.005$ a.u. case, due to the energy barrier on the PES of the $|\mathcal{E}_1\rangle$ state (Fig. S6b).

The adiabatic-Fock state population (open circles in Fig. S7b) for $g_c = 0.05$ a.u. becomes complicated. First, near the Franck-Condon region, besides the $|e0\rangle$ state, the $|e1\rangle$ state also contributes significantly to the $|\mathcal{E}_2\rangle$ state (Fig. S7b) due to the large permanent dipole of the $|e\rangle$ state. Second, during the dynamics, the $|e1\rangle$ state can either transform to the $|g1\rangle$ state through the CI between the $|e\rangle$ and $|g\rangle$ states or transform to the $|e2\rangle$ state through the light-matter coupling caused by the permanent dipole of the $|e\rangle$ state. Third, the $|g1\rangle$ state can further transform to the $|g2\rangle$ state through the light-matter coupling caused by the permanent dipole of the $|g\rangle$ state. As a result, we can observe that the $|e2\rangle$, $|g2\rangle$, and $|g1\rangle$ states are populated during the dynamics, especially at the early time. All of the above states as well as the $|e1\rangle$ state contribute to the photon number evolution, as shown in Fig. S7c. The population of the *trans* isomer shows a slight decrease (Fig. S7d) when compared to the dynamics outside the cavity since more trajectories oscillate around the *cis* configuration (Fig. S8b) as the Y-polarized case.

VII. CARTESIAN COORDINATES FOR SOME KEY CONFIGURATIONS

Ground-state minimum of the *Cis* isomer (optimized at the level of B3LYP/6-31G*)

<i>N</i>	0.00000	0.00000	0.00000
<i>N</i>	1.24304	0.00000	0.00000
<i>C</i>	-0.74229	0.00000	-1.28432
<i>C</i>	1.98532	-0.00016	-1.28433
<i>H</i>	-1.80740	-0.00305	-1.04833
<i>H</i>	-0.50818	0.89064	-1.88202
<i>H</i>	-0.50359	-0.88700	-1.88558
<i>H</i>	1.75109	-0.89080	-1.88199
<i>H</i>	1.74669	0.88685	-1.88561
<i>H</i>	3.05043	0.00280	-1.04835

Ground-state minimum of the *Trans* isomer (optimized at the level of B3LYP/6-31G*)

<i>N</i>	0.00000	0.00000	0.00000
<i>N</i>	1.24415	0.00000	0.00000
<i>C</i>	-0.56172	0.00000	-1.35571
<i>C</i>	1.80587	0.00005	1.35570
<i>H</i>	-1.20268	0.88407	-1.45418
<i>H</i>	0.21260	-0.00114	-2.13150
<i>H</i>	-1.20581	-0.88148	-1.45326
<i>H</i>	1.03155	0.00122	2.13150
<i>H</i>	2.44682	-0.88402	1.45421
<i>H</i>	2.44997	0.88153	1.45322

Conical intersection (optimized at the level of SA-2-CAS(6,4)/6-31G*)

<i>N</i>	0.00000	0.00000	0.00000
<i>N</i>	1.27667	0.00000	0.00000
<i>C</i>	-0.60803	0.00000	-1.32884
<i>C</i>	2.21900	-1.07580	0.08071
<i>H</i>	-1.62890	-0.34552	-1.23458
<i>H</i>	-0.61980	1.01460	-1.71124
<i>H</i>	-0.06100	-0.62909	-2.02451
<i>H</i>	2.09467	-1.62805	1.00824
<i>H</i>	2.11270	-1.76687	-0.75369
<i>H</i>	3.21377	-0.65580	0.05607

* Electronic address: deping.hu@rochester.edu

† Electronic address: pengfei.huo@rochester.edu

¹ A. Meurer, C. P. Smith, M. Paprocki, O. Čertík, S. B. Kirpichev, M. Rocklin, A. Kumar, S. Ivanov, J. K. Moore, S. Singh, et al., PeerJ Computer Science **3**, e103 (2017), ISSN 2376-5992, URL <https://doi.org/10.7717/peerj-cs.103>.

² Y. Zhang, T. Nelson, and S. Tretiak, J. Chem. Phys. **151**, 154109 (2019).

³ K. Bennett, M. Kowalewski, and S. Mukamel, Faraday Discuss. **194**, 259 (2016).

⁴ A. F. Kockum, A. Miranowicz, S. D. Liberato, S. Savasta, and F. Nori, Nature Rev. Phys. **1**, 19 (2019).

⁵ A. Mandal, S. M. Vega, and P. Huo, J. Phys. Chem. Lett. **11**, 9215 (2020).

⁶ C. Schäfer, M. Ruggenthaler, V. Rokaj, and A. Rubio, ACS Photonics **7**, 975 (2020).

⁷ E. A. Power and S. Zienau, Philos. Trans. Royal Soc. A **251**, 427 (1959).

⁸ C. Cohen-Tannoudji, J. Dupont-Roc, and G. Grynberg, *Photons and Atoms: Introduction to Quantum Electrodynamics* (Wiley, 1997), ISBN 978-0-471-18433-1, URL https://www.ebook.de/de/product/3737960/claude_cohen_tannoudji_jacques_dupont_roc_gilbert_grynberg_photons_and_atoms_introduction_to_quantum_electrodynamics.html.